AD-A230 112

DTIC FILE COPY

3-D Object Pose Determination
Using Complex F ⁻I

Sing Bing Kang and Katsushi Ikeuchi

CMU-RI-TR-90-18

DTIC
ELECTE
DEC 2 8 1990

The Robotics Institute
Carnegie Mellon University
Pittsburgh, Pennsylvania 15213

October 1990

90 12 27 059

REPORT DOCUMENTATION PAGE

Public reporting burden for this collection of information is estimated to average 1 hour per response, including the time for reviewing instructions, searching existing data sources, gathering and maintaining the data needed, and completing and reviewing the collection of information. Send comments regarding this burden estimate or any other aspect of this collection of information, including suggestions for reducing this burden, to Washington Headquarters Services, Directorate for Information Operations and Reports, 1215 Jefferson Davis Highway, Suite 1204, Arlington, VA 22202-4302, and to the Office of Management and Budget, Paperwork Reduction Project (0704-0188), Washington, DC 20503

1. AGENCY USE ONLY (Leave blank)	2. REPORT DATE	3. REPORT TYPE AND DATES COVERED
	October 1990	Technical

4. TITLE AND SUBTITLE

3-D Object Pose Determination Using Complex EGI

5. FUNDING NUMBERS

6. AUTHOR(S)

Sing Bing Kang and Katsushi Ikeuchi

7. PERFORMING ORGANIZATION NAME(S) AND ADDRESS(ES)

The Robotics Institute
Carnegie Mellon University
Pittsburgh, PA 15213

8. PERFORMING ORGANIZATION REPORT NUMBER

CMU-RI-TR-90-18

9. SPONSORING MONITORING AGENCY NAME(S) AND ADDRESS(ES)

DARPA

10. SPONSORING MONITORING AGENCY REPORT NUMBER

F33615-87-C-1499

11. SUPPLEMENTARY NOTES

12a. DISTRIBUTION AVAILABILITY STATEMENT

Approved for public release;
Distribution unlimited

12b. DISTRIBUTION CODE

13. ABSTRACT (Maximum 200 words)

This report describes a new method based on the Extended Gaussian Image (EGI) which can be used to determine the pose of a 3-D object. In this scheme, the weight associated with each outward surface normal is a complex weight. The normal distance of the surface from the predefined origin is encoded as the phase of the weight while the magnitude of the weight is the visible area of the surface. This approach decouples the orientation and translation determination into two distinct least-squares problems. Experiments involving synthetic data of two polyhedral and two smooth objects indicate the feasibility of this method. The best results are 4.7% and 1.5% (total distance error) for the polyhedral and smooth objects, respectively. The figures are quoted in terms of percentages of the maximum allowable displacement. Experiments using real range data for the two smooth objects yield good results, with total translation errors as low as 2.6%.

14. SUBJECT TERMS			15. NUMBER OF PAGES
			47
			16. PRICE CODE

17. SECURITY CLASSIFICATION OF REPORT	18. SECURITY CLASSIFICATION OF THIS PAGE	19. SECURITY CLASSIFICATION OF ABSTRACT	20. LIMITATION OF ABSTRACT
unlimited	unlimited	unlimited	

Contents

List of Figures

List of Tables

Abstract

This report describes a new method based on the Extended Gaussian Image (EGI) which can be used to determine the pose of a 3-D object. In this scheme, the weight associated with each outward surface normal is a complex weight. The normal distance of the surface from the predefined origin is encoded as the *phase* of the weight while the magnitude of the weight is the visible area of the surface. This approach decouples the orientation and translation determination into two distinct least-squares problems. Experiments involving synthetic data of two polyhedral and two smooth objects indicate the feasibility of this method. The best results are 4.7% and 1.5% (total distance error) for the polyhedral and smooth objects respectively. The figures are quoted in terms of percentages of the maximum allowable displacement. Experiments using real range data for the two smooth objects yield good results, with total translation errors as low as 2.6%.

Chapter 1

Introduction

A fundamental task in most 3-D computer vision and robotic systems is the determination of object pose in space. The pose of an object specifies completely its orientation and position with respect to a predefined frame or coordinate system.

There are two primary approaches to solve the pose determination problem: local and global. The local approach, typified by Faugeras [7] and Tanaka [21], seeks to match local features such as edges and curvature of surfaces and compute the linear transformation parameters from them. The global approach, on the other hand, does not rely on local and spatial correspondences to achieve this aim. It maps local features such as intensity, edge or area into an $\Re^n$-space where matching between the object and model is performed. Matching using the Hough transform and moment invariants are two examples in 2-D matching.

The Extended Gaussian Image (EGI) representation is an example of the global approach in 3-D space. The primary drawback of the EGI is the inability to determine the translation of a recognized 3-D object. This is because the weights in the EGI representation contain only area information and no positional data. One way to encode the positional information is to express the equation of the object face in dual space. This is the approach taken by Roach et al [20] who call the resulting encoded representation the *spherical dual image*. The dual space represents both the orientation and position of the planes or faces of the 3-D object; edges are explicitly described as connections between dual points. However, this scheme is primarily for object representation. Furthermore, planes passing near or through the designated origin cannot be dualized properly; they map to infinity or very large values.

This report describes a new representation called the Complex Extended Gaussian Image (CEGI) from which both the orientation and translation of a given 3-D object can be determined. In addition, the CEGI has the desirable property of being able to differentiate larger classes of objects than the conventional EGI.

1.1 Brief Description of the Complex EGI

The Complex EGI (CEGI) addresses the main deficiency of the conventional EGI, namely the inability to extract translation parameters. This is because the weight at each EGI cell is just

1

the sum of the area of the surface patches whose normal is associated with the cell. Thus the EGI weights are devoid of any direct positional information and are translation invariant.

The weight at each discrete cell of the CEGI is a complex number. The complex weight associated with a particular surface patch is determined as follows: The magnitude of the weight is the visible surface area of the object associated with its surface normal. The phase of each weight is the key to displacement determination; it is the (signed) distance of the surface patch from a designated origin in the direction of its normal.

By encoding the distance information this way, it can be easily shown that the magnitude of the total weight at each cell of the CEGI is independent of object position. Thus orientation can be determined in a manner identical to that for the conventional EGI. Once the orientation is found, the translation parameters can then be calculated by comparing the phases of the complex weights at matched cells of the model CEGI and the partial object CEGI.

Experiments were made to test the effectiveness of the CEGI concept in determining object translation. Two polyhedral models (one simple, the other relatively more complex in shape), and two smooth models (torus and ellipsoid) were employed in experiments involving synthesized data. To further validate and test out this concept, experiments involving real range data for the torus and ellipsoid were performed as well. The smallest error in total distance obtained in the simulations involving polyhedral objects is 4·7% while that for the smooth objects is 1·5%. For the experiments using real range data, the smallest error is 3·5%. The error figures are quoted in percentages of the maximum allowable displacement.

1.2 Organization of Report

Chapter 2 gives a brief description of the Extended Gaussian Image (EGI) and presents the proposed variant of the EGI, namely the Complex EGI or CEGI. It shows how the distance information can be encoded in the CEGI represetation.

The pose recovery strategy of a given object is subsequently presented in Chapter 3. Emphasis is especially made on how the translation parameters are determined, since this is the main advantage of CEGI over the conventional EGI representation. In addition, error analysis is made on the recovered translation factors. We also justify using a view suitability index as a measure of the translation parameter error bound.

Chapter 4 focuses on the results of simulations performed. There are two parts to this: In the first part, a set of simulations is made for both polyhedral and smooth objects to verify the feasibility of the CEGI as a means of extracting the displacement of the object. This is subsequently followed by the results obtained for the simulations made using the two polyhedral objects to verify the linear upper bound of translation errors.

The following chapter (Chapter 5) describes the experiments conducted using real range data and results obtained using the smooth models.

Final comments and conclusions are presented in Chapter 6.

1.3   Past Research on 3-D Object Pose Determination

Research on 3-D object pose determination has been intensive, but with varied results, as the comprehensive survey by Besl and Jain [2] indicates. This section is not intended to be exhaustive in its description of some of the research made in this area. It concentrates more on the research performed on pose determination for smooth 3-D objects. The motivation is clear: The world around us is composed of objects that are usually *not* piecewise planar, but rather smooth and continuous in nature.

Nevatia and Binford [18] match curved objects using generalized cylinders. Faugeras and Hebert [8], and Faugeras [6] have proposed a 3-D object recognition algorithm based on geometrical matching between primitive surfaces. The primitive surface that was actually implemented is the plane, though quadric surface algorithms are presented as well. The best accuracy quoted in [6] is 2.3 degrees for the rotation angle and 3 millimeters for the translation. The accuracy of the range data is 1 millimeter.

Bolles, Horaud and Hannah [3] developed 3DPO which recognizes and locates 3-D objects using range data. The system's hypothesis generation and matching is based on matching of several features or feature clusters involving object specific features such as a circular arc of a specific radius, and edges. Fan, Medioni and Nevatia [5], on the other hand, use surface descriptions such as jump boundaries, creases and limbs to match and locate 3-D objects. No accuracy figures were supplied in these two papers.

A recent paper by Ponce and Kreigman [19] describes a method to recognize and locate curved objects in a monocular intensity image. They consider the image contours, namely the projections of surface discontinuities and occluding contours, as the basis for recognition and location of the object. However, this assumes that the contour equations are parametrically known. Furthermore, the location of the object is estimated in the x-y plane only.

1.4   Past Research on the EGI

The EGI has been applied [12, 10] to determine the object attitude, where the rotation in 3-D space brings a sample object into correspondence with a prototype. It has also been used as a means of object recognition [11] in an industrial environment. The EGI of the visible portion of an unknown object is formed by a constrained optimization method applied to data from photometric stereo [13]. The prototype EGI which best matches the partial EGI identifies the object. Little [15] uses a variant of the EGI method which employs the mixed volume as a basis of attitude determination of the sensed object. The mixed volume is a geometric construction used in Minkowski's [16] proof of existence of a convex object given a valid EGI. This report addresses the deficiency faced by the normal EGI method, namely the inability to recover translation of objects.

In addition to recognizing objects and determining object attitude, the EGI has also been used to reconstruct convex polyhedra. Ikeuchi [13] has proposed a reconstruction precedure which minimizes the sum of the square differences between the calculated areas of the poly-hedron and the given area in the EGI. Little's iterative scheme [14] minimizes the error in the

area of the faces as well as in the location of the centroid of the reconstructed figure. More recently, Moni [17] has proposed a reconstruction method which involves determining the adjacency of faces and the length of edges of the polyhedron from the EGI.

Dane and Bajcsy [4] make use of the Gaussian Image to spatially segment a group of range points lying on a surface of a 3-D object into planar and quatric surfaces. The method proposed by Hebert and Ponce [9] segments depth maps into plane, cylindrical and conical primitives. This is done by mapping the estimated surface normals to the EGI and subsequently using the Hough transform to characterize the surfaces.

Chapter 2

The Complex EGI (CEGI)

2.1 Introduction to the EGI

The EGI of a 3-D object is a histogram which records the variation of surface area with surface orientation. The weights in the EGI representation do not contain any direct distance information. As such, it is translation invariant, and it is easy to see that the EGI representation rotates in the exact manner as the object in space. The EGI of a cube is shown in Fig. 2.1.

2.2 Description of the CEGI

In the conventional EGI representation, each weight associated with the normals of the object face are scalars which represent the associated visible face area. The CEGI (complex EGI) concept extends such a representation by adding the normal distance of that face to the origin (in the direction of the normal) as the *phase* component. This is illustrated in Fig. 2.2. In other words, the weight associated with a particular normal in the CEGI is a complex number whose magnitude is the corresponding visible face area and whose (signed) phase is the normal distance of the face from the designated origin in the direction of the normal. To illustrate further, in Fig 2.3, the complex weight associated with face A is $A_{\hat{n}_k} e^{jd_k}$, where $A_{\hat{n}_k}$ is the area of face A with the outward normal $\hat{n}_k$, and d_k is the normal distance of the plane Π_k (within which $A_{\hat{n}_k}$ lies) to an assigned origin. d_k is positive if the perpendicular vector from the origin to the face is in the same direction as the outward facing normal of the face. The value of d_k is positive in this case (Fig. 2.3).

For any given point in the CEGI corresponding to normal $\hat{n}_k$, the magnitude of the point's weight is $|A_{\hat{n}_k} e^{jd_k}|$. $A_{\hat{n}_k}$ is independent of the normal distance, and if the object is convex, the distribution of $A_{\hat{n}_k}$ corresponds to the conventional EGI representation. If the object is not convex, the magnitude of each weight will not necessarily be equal to those of the corresponding conventional EGI. This is an important attribute of the CEGI which will be further described in Section 2.3 in this chapter. The translation invariance property of the weight magnitude applies even if there are more than one contiguous surface patches with the

5

Gauss mapping

(a) Cube (b) EGI of cube

(Note: The weight is shown only for normal n_1 for clarity)
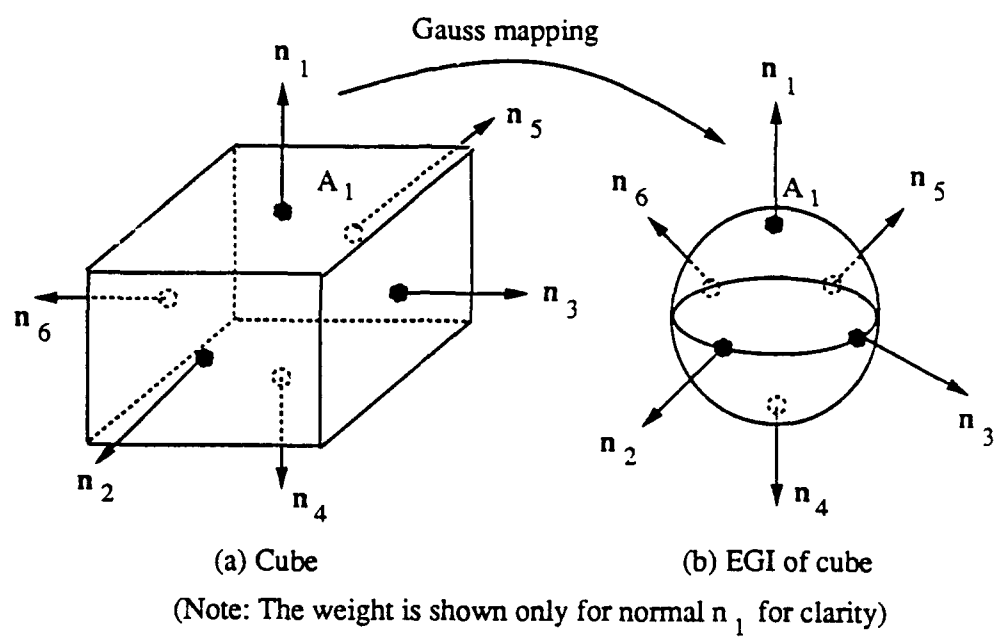
Figure 2.1: Illustration of the Extended Gaussian Image

Gauss mapping

(a) Cube (b) CEGI of cube

(Note: The weight is shown only for normal n_1 for clarity)
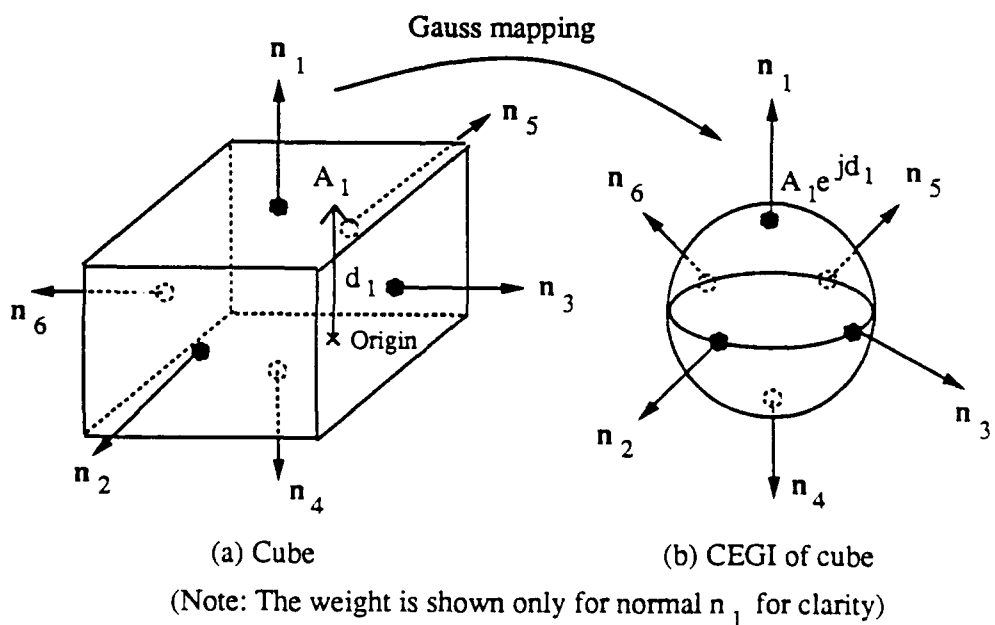
Figure 2.2: Illustration of the Complex Extended Gaussian Image

6

same outward normal. Consider surfaces whose normals are $\hat{n}_k$ (Fig. 2.4). Before translation, the corresponding complex weight is

$$\mathbf{P}_{\hat{n}_k} = \sum_{l=1}^{N_k} A_{l,\hat{n}_k} e^{jd_{lk}} \tag{2.1}$$

After a translation along a vector $\mathbf{T}$, the complex weight becomes

$$\mathbf{P}'_{\hat{n}_k} = \sum_{l=1}^{N_k} A_{l,\hat{n}_k} e^{j(d_{lk} + \mathbf{T} \cdot \hat{n}_k)} = e^{j\mathbf{T} \cdot \hat{n}_k} \mathbf{P}_{\hat{n}_k} \tag{2.2}$$

Hence for each point in the CEGI, the magnitude of the weight is independent of the translation. However, the complex number folds back onto itself for every magnitude change of 2π. Hence there exists an ambiguity range beyond which errors would occur. In our method, all distances are normalized such that the greatest expected change in distance is π.

So a change in the position in the same direction as the surface normal corresponds to a change in the phase component of the complex representation, without any change in its magnitude. Hence by comparing the magnitudes, we can then recognize objects and determine their orientations as we would for a conventional EGI. In addition, by comparing the differences in the complex weight phases, we can then proceed to calculate the distance change along the normals.

2.3 Representation of convex and non-convex objects

Another drawback of the conventional EGI is that it is possible for a convex object and a class of non-convex objects to have identical EGI's. CEGI's reduces this possibility. Consider the following two objects:

Suppose these two objects (one convex and the other non-convex) have identical EGI's. Comparing the weights associated with the normal in the positive z-direction, we have for object (1) (from Fig 2.5),

$$P_{1,\hat{k}} = A_1 e^{jd_1} \tag{2.3}$$

For object (2),

$$P_{2,\hat{k}} = A_{21} e^{jd_{21}} + A_{22} e^{jd_{22}} \tag{2.4}$$

Since they have identical EGI's, $A_1 = A_{21} + A_{22}$. Equating (2.3) to (2.4), we get

$$
\begin{aligned}
(A_{21} + A_{22})e^{jd_1} &= A_{21} e^{jd_{21}} + A_{22} e^{jd_{22}} \\
&= A_{21} \cos d_{21} + A_{22} \cos d_{22} + j(A_{21} \sin d_{21} + A_{22} \sin d_{22})
\end{aligned} \tag{2.5}
$$

For real values of d_1, d_2 and d_3, taking the square of the magnitudes,
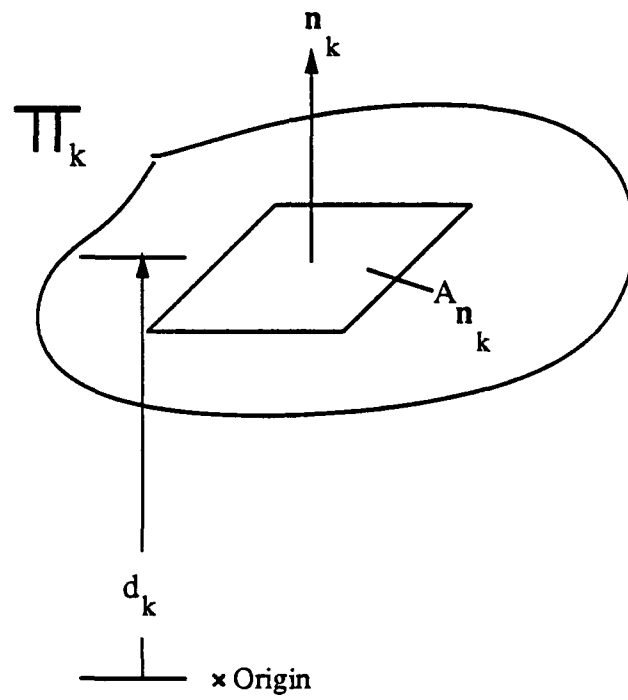
7

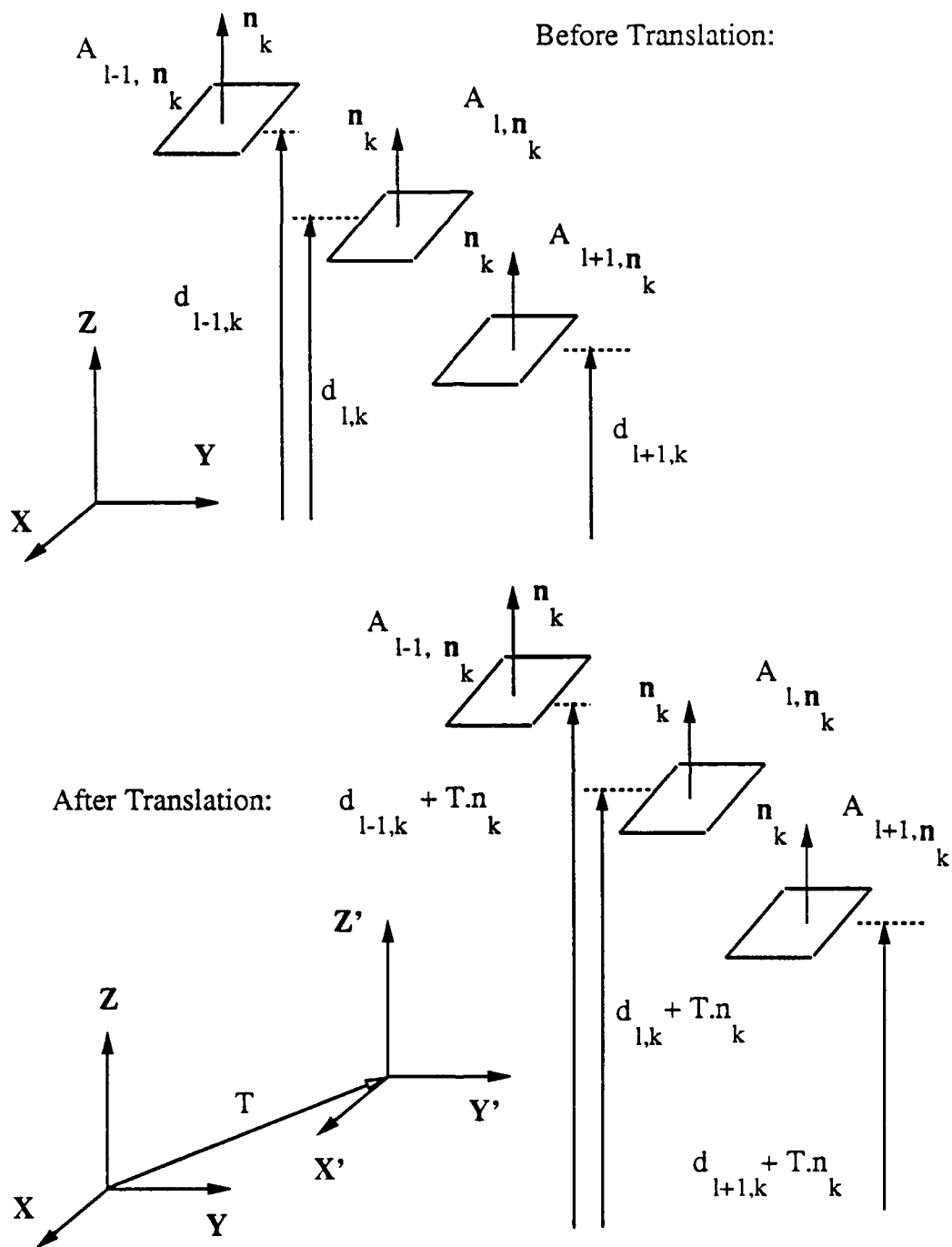Figure 2.3: Example of an oriented face with a complex weight $A_{n_k} e^{jd_k}$

Figure 2.4: Effect of translating object on the complex weight for particularly oriented faces
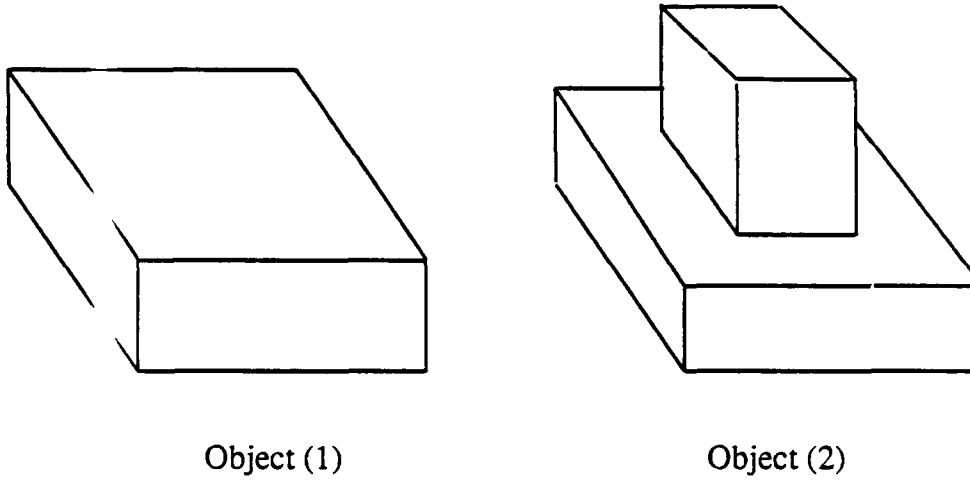
Object (1)   Object (2)

Figure 2.5: Example of two objects having identical EGI's

$$(A_{21} + A_{22})^2 = (A_{21} \cos d_{21} + A_{22} \cos d_{22})^2 + (A_{21} \sin d_{21} + A_{22} \sin d_{22})^2 \qquad (2.6)$$

$$\Rightarrow \quad \cos d_{21} \cos d_{22} + \sin d_{21} \sin d_{22} = 1 \qquad (2.7)$$

$$\Rightarrow \qquad \cos(d_{21} - d_{22}) = 1 \qquad (2.8)$$

Hence for $-\pi < d_{21}, d_{22} \le \pi$, $d_{21} = d_{22}$. In other words, the CEGI's of these two objects are different since there is no real solution for d_1 when $d_{21} \ne d_{22}$. This means that the CEGI is able to differentiate between convex and non-convex objects with identical EGI's.

For a given conventional EGI representation of an object, the center of mass coincides with the sphere center. If $P_{\hat{n}_i}^{EGI}$ is the weight at normal $\hat{n}_i$, then the previous statement can be mathematically expressed as

$$\sum_{i=1}^{N_{faces}} P_{\hat{n}_i}^{EGI} \hat{n}_i = 0 \qquad (2.9)$$

where N_{faces} is the number of flat surfaces. For the CEGI representation, this is not always true. In fact, for any given model, if

$$\sum_{i=1}^{N_{faces}} |P_{\hat{n}_i}^{CEGI}| \hat{n}_i \ne 0 \qquad (2.10)$$

then that object is *not* convex. This follows from the expression $\sum |P_{\hat{n}_i}^{CEGI}| \hat{n}_i$ being the analogous CEGI's "center of mass" for the object. On the other hand, if $\sum |P_{\hat{n}_i}^{CEGI}| \hat{n}_i = 0$, then it does not necessarily mean that the object is convex. This relation is a necessary but not sufficient condition for convexity. A point symmetric non-convex object as shown in Fig. 2.6
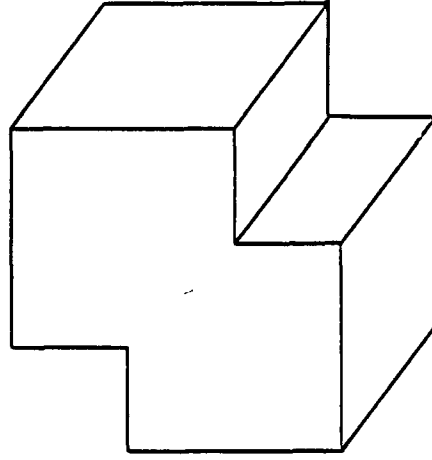
10

Figure 2.6: A point symmetric object

or objects depicted in Fig. 2.7 satisfy the condition $\sum |P_{\hat{n}_i}^{CEGI}|\hat{n}_i = 0$. Note that for the objects in Fig. 2.7, each face has a unique outward normal. This accounts for the satisfaction of the condition $\sum |P_{\hat{n}_i}^{CEGI}|\hat{n}_i = 0$ in these cases.

Assuming the object is not point symmetric, non-convex and satisfies the relation $\sum |P_{\hat{n}_i}^{CEGI}|\hat{n}_i = 0$, then at least one of the following conditions must be satisfied:

1. The non-convex parts of the object possess face gradients not found elsewhere. In other words, each face must have a unique outward normal. Examples of such objects are shown in Fig. 2.7; and

2. If the non-convex parts of the object contain faces with the same gradients as those at other parts, then these faces must lie on the same plane, i.e. they have the same normal distance from the origin.

Proving condition (2) above is equivalent to showing that if

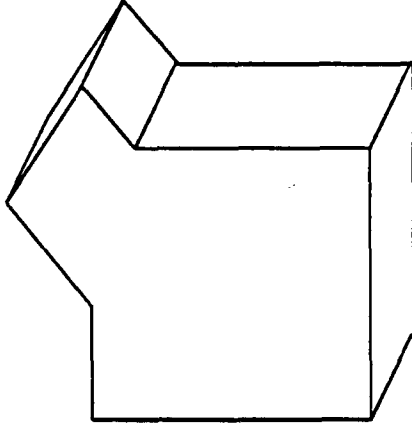$$\sum_{i=1}^{n} a_i e^{jd_i} = e^{jd_0} \sum_{i=1}^{n} a_i, \ a_i, d_i, d_0 \text{ being real.} \tag{2.11}$$

then $d_i = d_0$, i = 1, ..., n. To show this, taking the magnitude of both side of (2.11),

$$|\sum_{i=1}^{n} a_i e^{jd_i}| = \sum_{i=1}^{n} a_i \tag{2.12}$$

Using the triangle inequality for the LHS of (2.12),

$$|\sum_{i=1}^{n} a_i e^{jd_i}| \leq \sum_{i=1}^{n} |a_i e^{jd_i}| = \sum_{i=1}^{n} a_i, \text{ since } a_i \geq 0, \ i = 1, \dots, n \tag{2.13}$$

Hence the equality holds only if and only if d_i, i = 1, ..., n are all equal to one another. Equating the phase components, we get $d_i = d_0$, i = 1, ..., n.

11
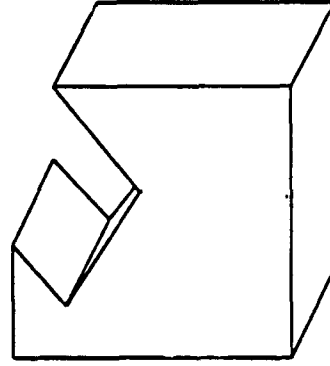
Figure 2.7: Examples of non-convex objects satisfying the relation $\sum |P^{CEGI}_{\hat{n}_i}|\hat{n}_i = 0$

Chapter 3

Pose Determination Strategy Using CEGI

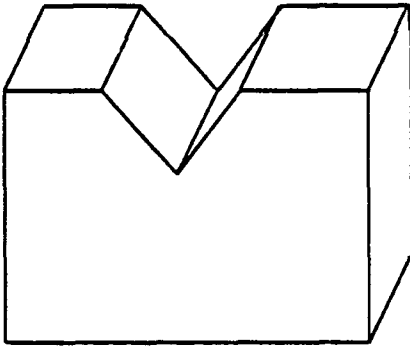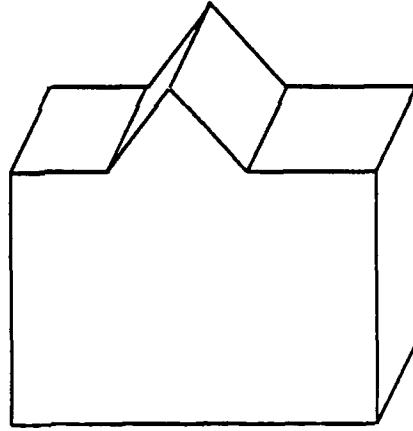## 3.1 Methodology

Given a prototype CEGI and a partial CEGI of an unknown object, we can recognize the object and determine its orientation by the following: first, calculating the magnitude distributions of both CEGI's and second, proceeding as one would for the conventional EGI's. Once both the object and its orientation with respect to the stored model are recognized, the object translation can be calculated by using the suitably oriented CEGI's.

The translation parameters can be determined by applying a least-squares technique as follows: Suppose that the object has been translated by δx, δy and δz in the x-, y- and z-directions respectively (in the model world coordinates). Then for each surface whose surface normal is $\hat{n}_k$, and whose complex weight is originally $A_{\hat{n}_k} e^{jd_k}$, after translation, the complex weight becomes $A_{\hat{n}_k} e^{j(d_k + \delta d \cdot \hat{n}_k)}$, where

$$
\begin{aligned}
\delta \mathbf{d} &= \delta x \hat{\mathbf{i}} + \delta y \hat{\mathbf{j}} + \delta z \hat{\mathbf{k}} \\
\hat{n}_k &= n_{kx} \hat{\mathbf{i}} + n_{ky} \hat{\mathbf{j}} + n_{kz} \hat{\mathbf{k}}
\end{aligned}
\tag{3.1}
$$

Then for each matched weight $P'_{\hat{n}_i}$ in the object CEGI corresponding to the weight $P_{\hat{n}_i}$ in the model CEGI, let

$$
\begin{aligned}
\omega_i &= \arg\left(\frac{P'_{\hat{n}_i}}{P_{\hat{n}_i}}\right) \\
&= \arg\left(\frac{A_{\hat{n}_k} e^{j(d_k + \delta d \cdot \hat{n}_k)}}{A_{\hat{n}_k} e^{jd_k}}\right) \\
&= \delta x n_{ix} + \delta y n_{iy} + \delta z n_{iz} \\
&\quad \text{for } i = 1, \ldots, N_{visible}
\end{aligned}
\tag{3.2}
$$

where $N_{visible}$ is the total number of visible faces on the object. We try to minimize the total squared error given by

$$\mathcal{E} = \sum_{i=1}^{N_{visible}} (\omega_i - n_{ix}\delta x - n_{iy}\delta y - n_{iz}\delta z)^2 \tag{3.3}$$

This is done by differentiating $\mathcal{E}$ with respect to the three unknown translation parameters and equating them to zero, i.e.

$$\frac{\partial \mathcal{E}}{\partial \delta x} = \frac{\partial \mathcal{E}}{\partial \delta y} = \frac{\partial \mathcal{E}}{\partial \delta z} = 0 \tag{3.4}$$

which yield the following system of equations:

$$
\begin{aligned}
\delta x \sum n_{ix}^2 + \delta y \sum n_{ix}n_{iy} + \delta z \sum n_{ix}n_{iz} &= \sum \omega_i n_{ix} \\
\delta x \sum n_{ix}n_{iy} + \delta y \sum n_{iy}^2 + \delta z \sum n_{iy}n_{iz} &= \sum \omega_i n_{iy} \\
\delta x \sum n_{ix}n_{iz} + \delta y \sum n_{iy}n_{iz} + \delta z \sum n_{iz}^2 &= \sum \omega_i n_{iz}
\end{aligned}
\tag{3.5}
$$

Using Cramer's rule to solve for δx, δy and δz, we get

$$\delta x = \frac{1}{D} \begin{vmatrix} \sum \omega_i n_{ix} & \sum n_{ix}n_{iy} & \sum n_{ix}n_{iz} \\ \sum \omega_i n_{iy} & \sum n_{iy}^2 & \sum n_{iy}n_{iz} \\ \sum \omega_i n_{iz} & \sum n_{iy}n_{iz} & \sum n_{iz}^2 \end{vmatrix} \tag{3.6}$$

$$\delta y = \frac{1}{D} \begin{vmatrix} \sum n_{ix}^2 & \sum \omega_i n_{ix} & \sum n_{ix}n_{iz} \\ \sum n_{ix}n_{iy} & \sum \omega_i n_{iy} & \sum n_{iy}n_{iz} \\ \sum n_{ix}n_{iz} & \sum \omega_i n_{iz} & \sum n_{iz}^2 \end{vmatrix} \tag{3.7}$$

$$\delta z = \frac{1}{D} \begin{vmatrix} \sum n_{ix}^2 & \sum n_{ix}n_{iy} & \sum \omega_i n_{ix} \\ \sum n_{ix}n_{iy} & \sum n_{iy}^2 & \sum \omega_i n_{iy} \\ \sum n_{ix}n_{iz} & \sum n_{iy}n_{iz} & \sum \omega_i n_{iz} \end{vmatrix} \tag{3.8}$$

where

$$D = \begin{vmatrix} \sum n_{ix}^2 & \sum n_{ix}n_{iy} & \sum n_{ix}n_{iz} \\ \sum n_{ix}n_{iy} & \sum n_{iy}^2 & \sum n_{iy}n_{iz} \\ \sum n_{ix}n_{iz} & \sum n_{iy}n_{iz} & \sum n_{iz}^2 \end{vmatrix} \tag{3.9}$$

In order for this scheme to work, the magnitude of the translation (i.e the normalized translation) must be less than π as given in (3.10).

$$\Delta = \sqrt{(\delta x)^2 + (\delta y)^2 + (\delta z)^2} < \pi \tag{3.10}$$

This is because the complex weight is unique as long as the phase (and hence the normal distance of the surface from the origin) lies within the principal interval $(-\pi, \pi]$.

3.2   Analysis of Error in Translation Parameters

The upper bound error depends on a variety of parameters, with the main factors being the normal and normal distance errors. Curiously enough, for a *convex* object, the magnitude of the weight does not contribute to the distance error. This is because only the *phase* components of the complex weight are used in the least square formulation, and for a convex object, no complex weight associated with a particular normal is a combination of at least two weights from two different disjoint object faces.

Each normal is represented by its directional cosines

$$\hat{\mathbf{n}}_l = (\cos\theta_{x,l} \ \cos\theta_{y,l} \ \cos\theta_{z,l})^T \tag{3.11}$$

and is subject to the constraint

$$\cos^2\theta_{x,l} + \cos^2\theta_{y,l} + \cos^2\theta_{z,l} = 1 \tag{3.12}$$

Suppose the exact translation is $\delta\mathbf{d} = (\delta x \ \delta y \ \delta z)^T$ and the approximated translation obtained using the least square formulation is $\delta\mathbf{d}' = (\delta x' \ \delta y' \ \delta z')^T$. In addition, suppose that the perturbed l^{th} normal is indicated by $\hat{\mathbf{n}}'_l$. Let

$$\omega_l = \arg\left(\frac{P_{\hat{\mathbf{n}}_{l,obj}}}{P_{\hat{\mathbf{n}}_{l,model}}}\right) \tag{3.13}$$

i.e.

$$
\begin{aligned}
\omega_l &= \delta\mathbf{d} \cdot \hat{\mathbf{n}}_l \\
&= \delta x \cos\theta_{x,l} + \delta y \cos\theta_{y,l} + \delta z \cos\theta_{z,l}
\end{aligned} \tag{3.14}
$$

For an imperfectly extracted object,

$$
\begin{aligned}
\omega_l + \epsilon_l &= \delta\mathbf{d}' \cdot \hat{\mathbf{n}}'_l \\
&= \delta x' \cos\theta'_{x,l} + \delta y' \cos\theta'_{y,l} + \delta z' \cos\theta'_{z,l} \\
&= (\delta x + \epsilon_x)\cos(\theta_{x,l} + \eta_{x,l}) + (\delta y + \epsilon_y)\cos(\theta_{y,l} + \eta_{y,l}) + \\
&\quad (\delta z + \epsilon_z)\cos(\theta_{z,l} + \eta_{z,l})
\end{aligned} \tag{3.15}
$$

Subtracting (3.14) from (3.15) and ignoring the second order terms, we have

$$\epsilon_l = \epsilon_x \cos\theta_{x,l} - \eta_{x,l}\delta x \sin\theta_{x,l} + \epsilon_y \cos\theta_{y,l} - \eta_{y,l}\delta y \sin\theta_{y,l} + \epsilon_z \cos\theta_{z,l} - \eta_{z,l}\delta z \sin\theta_{z,l} \tag{3.16}$$

Hence

$$
\begin{aligned}
\epsilon_x \cos\theta_{x,l} \ &+ \ \epsilon_y \cos\theta_{y,l} + \epsilon_z \cos\theta_{z,l} \\
&= \epsilon_l + \eta_{x,l}\delta x \sin\theta_{x,l} + \eta_{y,l}\delta y \sin\theta_{y,l} + \eta_{z,l}\delta z \sin\theta_{z,l}
\end{aligned} \tag{3.17}
$$

15

Suppose that the maximum positive error is $|\eta_{x,l}|_{max} = |\eta_{y,l}|_{max} = |\eta_{z,l}|_{max} = \eta_{max}$. For the normalized distances, $|\delta x|_{max} = |\delta y|_{max} = |\delta z|_{max} = \pi$. The following simplifying assumptions are made:

1. The normals can be "mapped" into the first octant; x, y and z values are positive such that the smaller angle subtended with the x, y and z axes are still the same. This means that $0 \le \theta_{x,l}, \theta_{y,l}, \theta_{z,l} \le \frac{\pi}{2}$;

2. $\epsilon_x, \epsilon_y, \epsilon_z$, and ϵ_l are all positive.

Then,

$$
\begin{aligned}
|\epsilon_x| \cos \theta_{x,l} \quad + \quad & |\epsilon_y| \cos \theta_{y,l} + |\epsilon_z| \cos \theta_{z,l} \\
\le \quad & |\epsilon_l| + \eta_{max}\pi(\sin \theta_{x,l} + \sin \theta_{y,l} + \sin \theta_{z,l})
\end{aligned}
\tag{3.18}
$$

Summing this over all the visible normals and averaging, we obtain

$$
|\epsilon_x|\kappa_{\theta x} + |\epsilon_y|\kappa_{\theta y} + |\epsilon_z|\kappa_{\theta z} \le \xi + \eta_{max}\pi(\tau_{\theta x} + \tau_{\theta y} + \tau_{\theta z})
\tag{3.19}
$$

where

$$
\kappa_{\theta x} = \frac{1}{N_{visible}} \sum_{l=1}^{N_{visible}} \cos \theta_{x,l}
$$

$$
\kappa_{\theta y} = \frac{1}{N_{visible}} \sum_{l=1}^{N_{visible}} \cos \theta_{y,l}
$$

$$
\kappa_{\theta z} = \frac{1}{N_{visible}} \sum_{l=1}^{N_{visible}} \cos \theta_{z,l}
$$

$$
(0 \le \theta_{x,l}, \theta_{y,l}, \theta_{z,l} \le \frac{\pi}{2})
$$

$$
\xi = \frac{1}{N_{visible}} \sum_{l=1}^{N_{visible}} |\omega_l - \hat{\mathbf{n}}_l' \cdot (\delta x' \delta y' \delta z')^T|
\tag{3.20}
$$

$$
\tau_{x,l} = \frac{1}{N_{visible}} \sum_{l=1}^{N_{visible}} \sin \theta_{x,l}
$$

$$
\tau_{y,l} = \frac{1}{N_{visible}} \sum_{l=1}^{N_{visible}} \sin \theta_{y,l}
$$

$$
\tau_{z,l} = \frac{1}{N_{visible}} \sum_{l=1}^{N_{visible}} \sin \theta_{z,l}
$$

The value of ξ is normally small when compared to the other terms (at least an order of magnitude smaller) and thus can be ignored. From (3.19), we can deduce the following set of constraints on the maximum error in each direction:

$$|\epsilon_x| \leq \frac{\eta_{max}\pi(\tau_{\theta x} + \tau_{\theta y} + \tau_{\theta z})}{\kappa_{\theta x}}$$

$$|\epsilon_y| \leq \frac{\eta_{max}\pi(\tau_{\theta x} + \tau_{\theta y} + \tau_{\theta z})}{\kappa_{\theta y}} \qquad (3.21)$$

$$|\epsilon_z| \leq \frac{\eta_{max}\pi(\tau_{\theta x} + \tau_{\theta y} + \tau_{\theta z})}{\kappa_{\theta z}}$$

From the set of inequalities (3.22), the constraint on the error in the total effective distance is

$$\epsilon_{total} = \sqrt{\epsilon_x^2 + \epsilon_y^2 + \epsilon_z^2}$$

$$\leq \eta_{max}\pi(\tau_{\theta x} + \tau_{\theta y} + \tau_{\theta z})\sqrt{\frac{1}{\kappa_{\theta x}^2} + \frac{1}{\kappa_{\theta y}^2} + \frac{1}{\kappa_{\theta z}^2}} \qquad (3.22)$$

Define the view suitability index

$$\Omega_\theta = (\tau_{\theta x} + \tau_{\theta y} + \tau_{\theta z})\sqrt{\frac{1}{\kappa_{\theta x}^2} + \frac{1}{\kappa_{\theta y}^2} + \frac{1}{\kappa_{\theta z}^2}} \qquad (3.23)$$

so that

$$\epsilon_{total} \leq \eta_{max}\pi\Omega_\theta \qquad (3.24)$$

This index shows us that minimizing the distance error *bound* requires us to find a viewpoint having it as its minimum. (3.24) indicates that the error bound increases linearly as a function of the view suitability index Ω_θ.

.

Chapter 4

Simulations

4.1 Experiments Involving Polyhedral Objects

Two models are used to test the concept of translation parameter extraction using the CEGI representation; they are shown in Fig. 4.2 and Fig. 4.3.

4.1.1 Implementational Issues

The scheme was implemented in Lisp, with the models generated using VANTAGE. VANTAGE is a geometric/sensor modeler developed at Carnegie Mellon University [1]. The CEGI viewing sphere is discretized into 240 sampling view directions located at the center of each face of the 2-frequency dodecahedron (tesselated pentakis dodecahedron) as shown in Fig. 4.1. The normal direction space is discretized into 240 cells as well. The CEGI weights are re-computed for each discrete view direction. This is to compensate for the varying degrees of self-occlusion which causes non-convex objects to register different weights at different view directions for the same surface normal.

4.1.2 Results

The results of the simulation are depicted in Fig. 4.4 and Fig. 4.5. As can be seen, Model 1 evinces a higher variability in errors than those demonstrated with Model 2. The extremely high peaks in Fig. 4.4 correspond to errors detected when the actual viewpoint subtends a very small angle to the x-y plane. Since the planes which yield the z-direction information (i.e. perpendicular to the z-axis) for Model 1 (shown in Fig. 4.2) subtend almost 90 degrees to these viewpoints, errors predicted in the z-direction are not reliable and are prone to high errors. In addition, Model 1 has fewer faces than Model 2 (shown in Fig. 4.3). Furthermore, the number of differently oriented normals in Model 1 is even smaller than those in Model 2.

Table 4.1 summarizes the simulation results for the two polyhedral objects. All the errors are expressed in percentages of the maximum displacement. (Note: $\overline{\epsilon_K}$ denotes the average error in K while σ_{ϵ_K} is the standard deviation of the error distribution.)
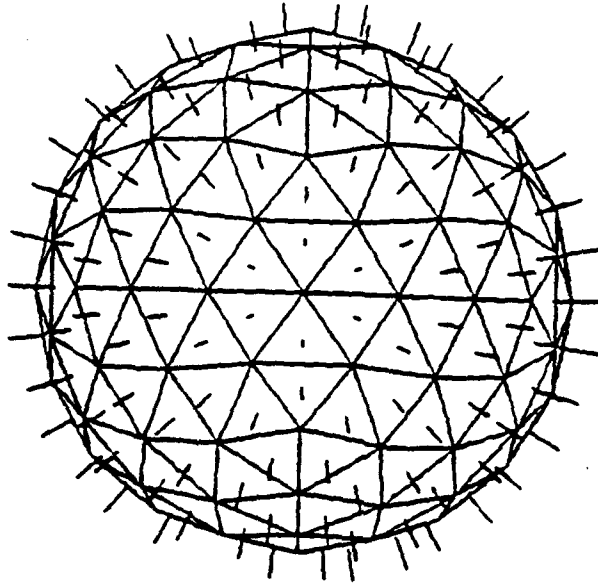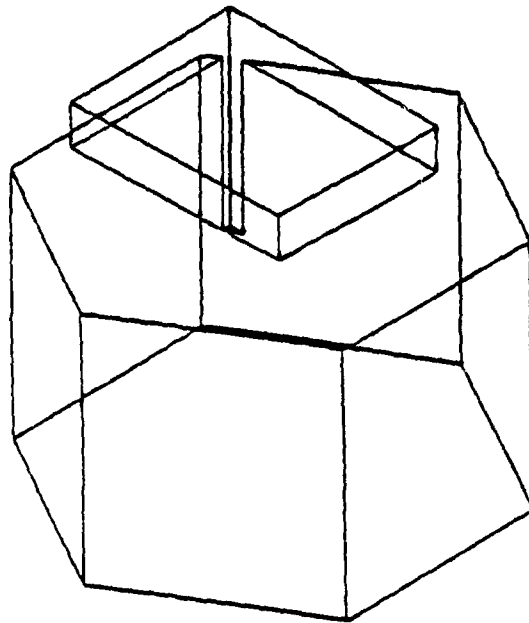
18

Figure 4.1: Tesselated pentakis dodecahedron
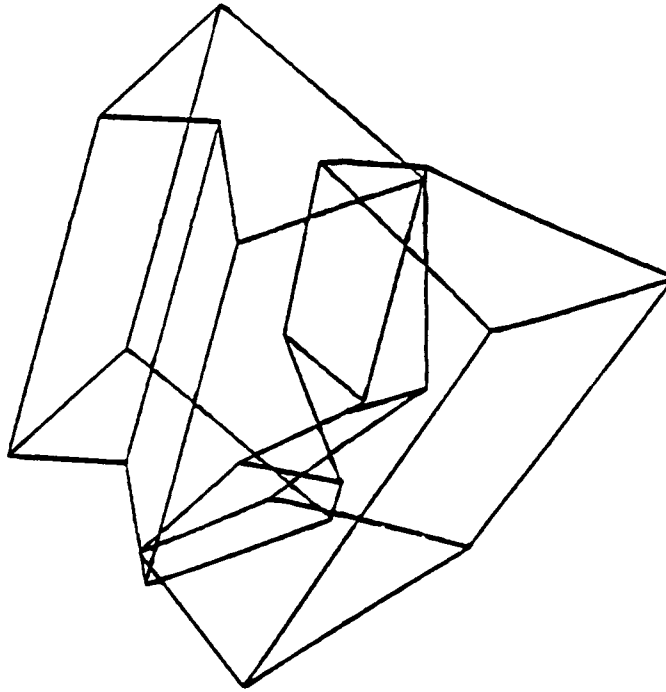
Figure 4.2: First composite object used for testing

Figure 4.3: Second composite object used for testing

Model #	$\bar{e}_{d_x}$	$\sigma_{e_{d_x}}$	$\bar{e}_{d_y}$	$\sigma_{e_{d_y}}$	$\bar{e}_{d_z}$	$\sigma_{e_{d_z}}$	$\bar{e}_{d_{xyz}}$	$\sigma_{e_{d_{xyz}}}$
1	1.6	1.2	3.4	3.8	12.2	15.9	14.1	16.3
2	2.5	1.8	2.6	1.8	2.1	1.7	4.7	2.3

Table 4.1: Results for Simulations Involving Polyhedral Objects

It can be readily seen from Table 4.1 that Model 1 yields significantly higher predicted distance errors than Model 2. For Model 1, if the viewpoint subtends a very small angle to the either the z-axis or the x-y plane, the errors incurred in the recovery will be very high; this is attributed to the sparse and uneven distribution of Model 1's normals. On the other hand, the number of different surface normals and their more even distribution result in lower errors in the recovered parameters, as evidenced in the results for Model 2.

4.2 Experiments Involving Smooth Objects

In addition to the two polyhedral objects, two smooth and continuous objects were also used in simulations and experiments involving real range data. The two chosen smooth objects are the torus and the ellipsoid (Fig. 4.6).
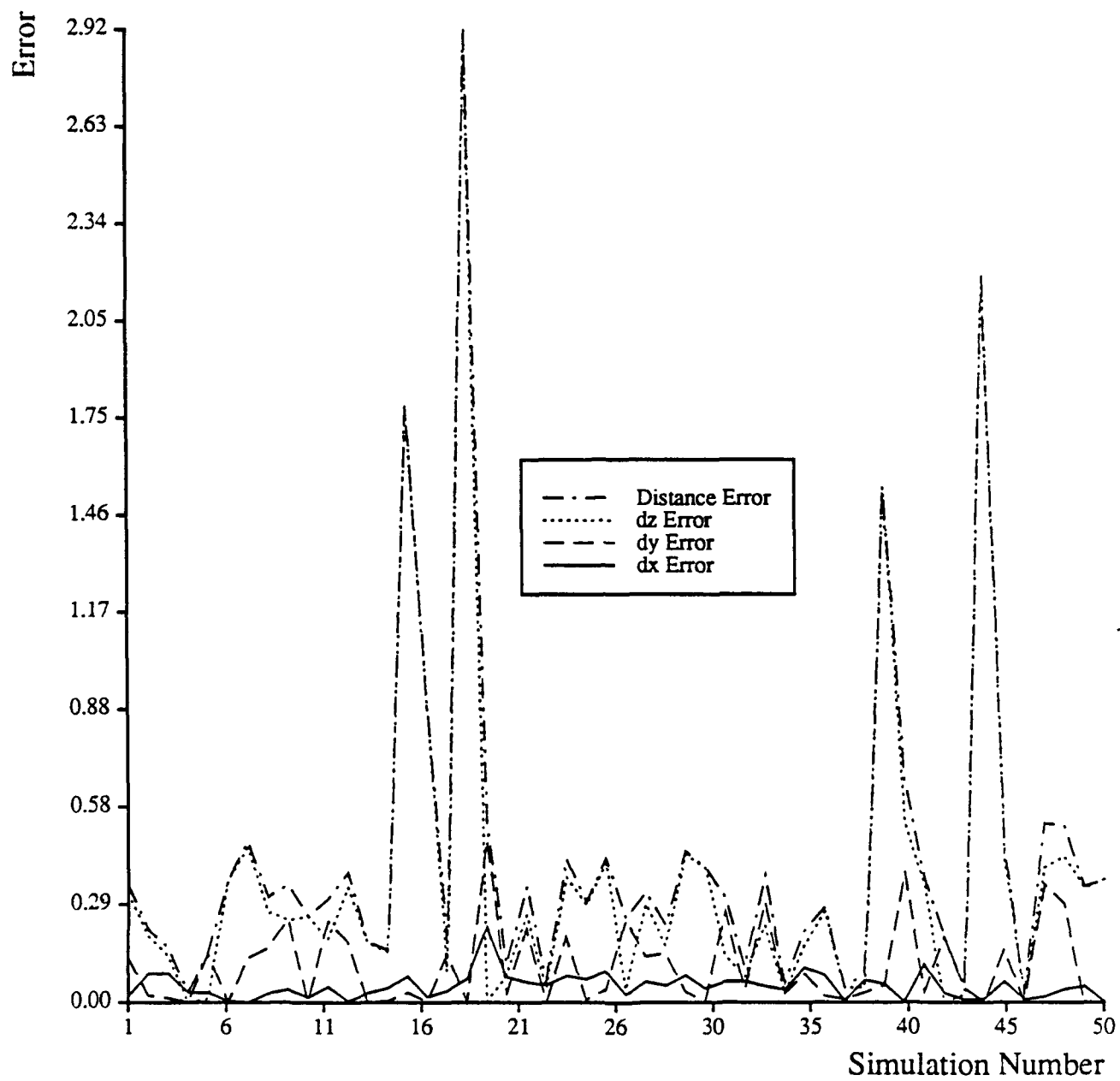
20

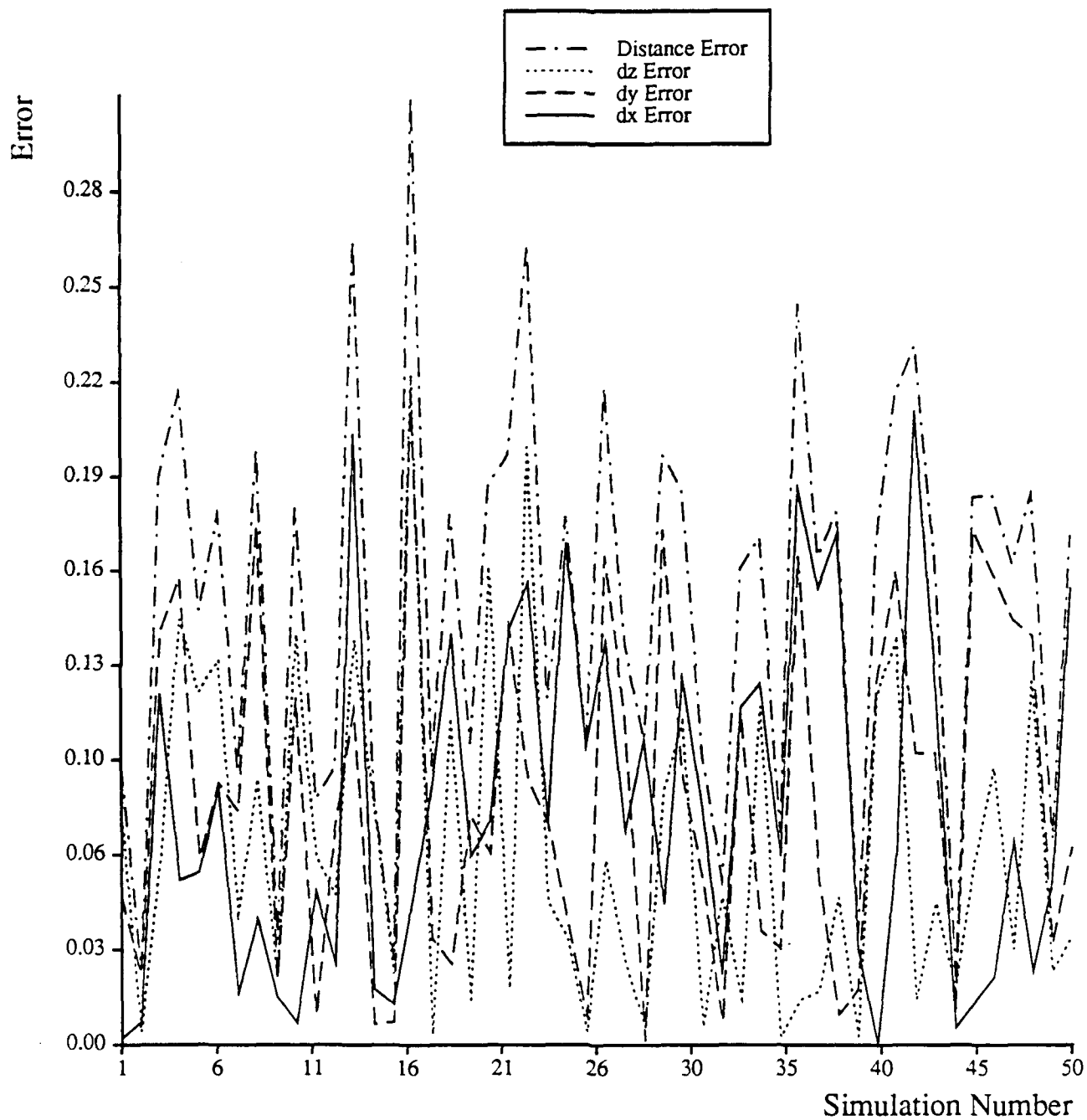Figure 4.4: Errors in dx, dy, dz and Total Distance for Model 1

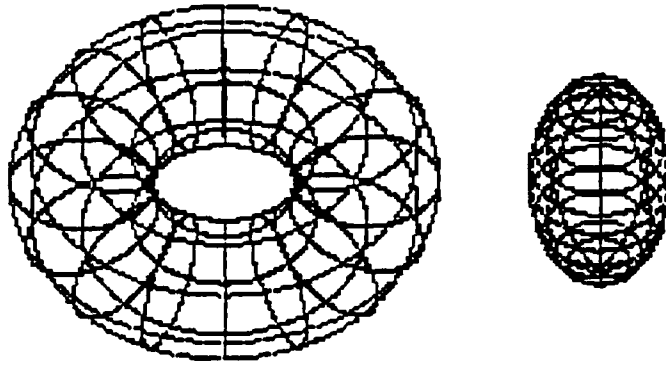Figure 4.5: Errors in dx, dy, dz and Total Distance for Model 2

Figure 4.6: Models used in experiments: torus (left) and ellipsoid (right)

4.2.1 Simulation

Implementational Issues

The torus is modeled parametrically as $[(R+r\cos\theta)\cos\phi, (R+r\cos\theta)\sin\phi, r\sin\theta]^T$ while the ellipsoid is represented parametrically as $[a\sin\theta\cos\phi, a\sin\theta\sin\phi, b\cos\theta]^T$. The ideal setup is shown in Fig. 4.7. The parametric values used are: r=20, R=40, a=20, b=40, $|O_IO|$=100, and $|V_cO|$=1000. Simulations are performed for image resolutions n×n for n = 32, 64 and 128.

To achieve a certain degree of realism, a simple ray-tracing technique is employed to estimate the object surface area projected onto each pixel as well as the surface normal to be attributed to that surface. This is illustrated in Fig. 4.8. The surface normal is approximated to be that at point P_{ck} while the surface area is estimated by the sum of the area of the triangles $\Delta P_{ck}P_{1k}P_{2k}$, $\Delta P_{ck}P_{2k}P_{3k}$, $\Delta P_{ck}P_{3k}P_{4k}$ and $\Delta P_{ck}P_{4k}P_{1k}$. If the surface normal is n_k and the area is A_k, then the complex weight attributed to this surface is simply $A_k e^{jn_k \cdot P_{ck}}$. This is done for all the pixels in the image plane.

Results

The simulation results are graphically depicted in Fig. 4.9 and listed in Tables 4.2 and 4.3. The number of runs for each resolution per object is 250. For both of these models, it is apparent that the errors in the predicted displacement decreases monotonically as the resolution increases.

We also observe that the displacement errors incurred for the torus are significantly higher (a factor of about 2-3) than those incurred for the ellipsoid. This phenomena can be readily explained as follows:

Since the ellipsoid is convex, the resultant complex weight in each CEGI cell is the sum of those weights corresponding to surface patches which are either contiguous or spatially close to each other. (The number of contributing surface patches to a cell is inversely proportional to the local Gaussian curvature.) As such, the phases of these contributing complex weights are not expected to be very different from each other, despite errors in the phases. Since the resultant phase must lie between the minimum and maximum of these phases, the variance of the resultant phase error is expected to be small.
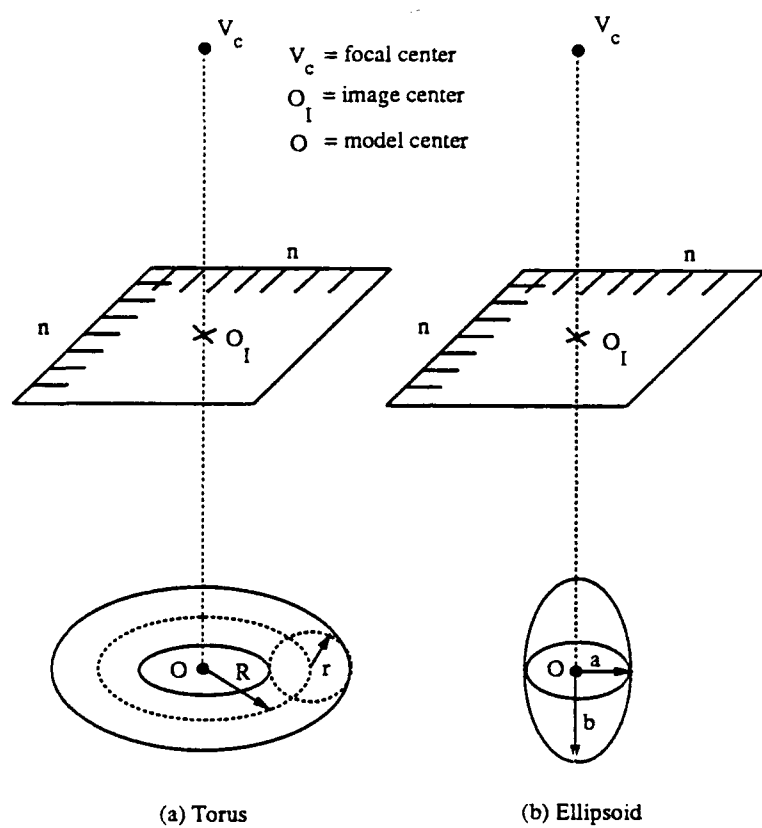
23

V_c = focal center

O_I = image center

O = model center

(a) Torus   (b) Ellipsoid

Figure 4.7: Simulation using the torus (left) and ellipsoid (right). n denotes the resolution in the x- and y- directions of the simulated image plane.
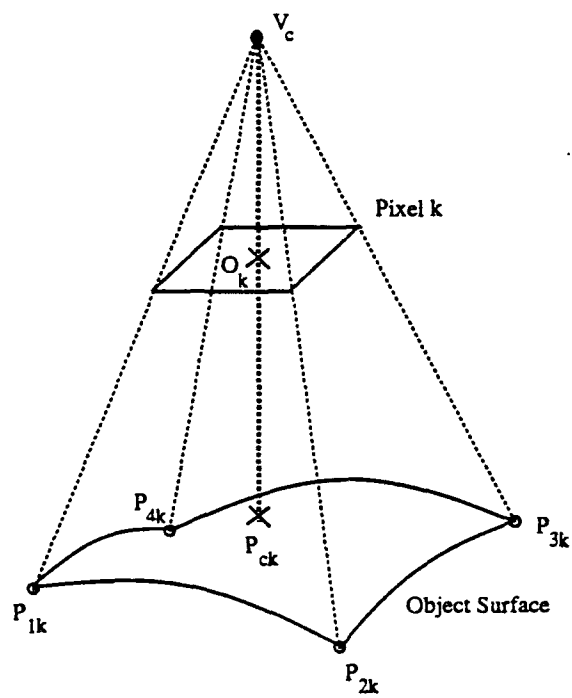
24

Figure 4.8: Approximation of area and surface normal in simulation

Resolution	$\bar{\epsilon}_{d_x}$	$\sigma_{\epsilon_{d_x}}$	$\bar{\epsilon}_{d_y}$	$\sigma_{\epsilon_{d_y}}$	$\bar{\epsilon}_{d_z}$	$\sigma_{\epsilon_{d_z}}$	$\bar{\epsilon}_{d_{xyz}}$	$\sigma_{\epsilon_{d_{xyz}}}$
32×32	5.0	5.5	5.6	6.1	3.9	3.3	9.9	7.3
64×64	3.2	3.2	3.5	3.7	2.5	2.0	6.3	4.1
128×128	1.4	1.5	1.3	1.2	1.3	1.1	2.7	1.7

Table 4.2: Simulation Results for Torus

Resolution	$\bar{\epsilon}_{d_x}$	$\sigma_{\epsilon_{d_x}}$	$\bar{\epsilon}_{d_y}$	$\sigma_{\epsilon_{d_y}}$	$\bar{\epsilon}_{d_z}$	$\sigma_{\epsilon_{d_z}}$	$\bar{\epsilon}_{d_{xyz}}$	$\sigma_{\epsilon_{d_{xyz}}}$
32×32	1.1	1.1	1.0	0.8	1.8	1.5	2.7	1.5
64×64	0.8	0.8	0.8	0.7	1.5	1.1	2.1	1.1
128×128	0.5	0.4	0.5	0.3	1.2	1.0	1.5	0.9

Table 4.3: Simulation Results for Ellipsoid

On the other hand, for the non-convex torus, this is not true. Two spatially distinct groups of surface patches, whose normal distances differ greatly, may contribute to a cell in the CEGI. The phase of the resultant complex weight is thus expected to have higher variability than that for the ellipsoid, for the same amount of phase error per surface patch.

4.3 Verification of the View Suitability Index

The previous chapter establishes the upper bound relationship between errors in the distances δ_x, δ_y, δ_z, the total effective distance, and the view suitability index. Simulations were made to verify this linear relationship. To simplify the analysis, we considered the case where the normals are not discretized according to the pentakis dodecahedron. Instead, normals are represented exactly. Random positional errors, which are subject to certain specified angular errors between the actual and randomized normals, are created to simulate the errors that could occur in a real situation. Since Fig.s 4.14-4.16 and Fig.s 4.21-4.22 show that the distance errors do indeed increase in a linear fashion with the angular error, we are able to use the view suitability index as a means of comparison. Furthermore, as Fig.s 4.10-4.13 and Fig.s 4.17-4.20 show, the view suitability index Ω_θ does appear to be a reasonable means of determining the upper bound of the distance errors in the x-, y-, z-, and effective total distances.
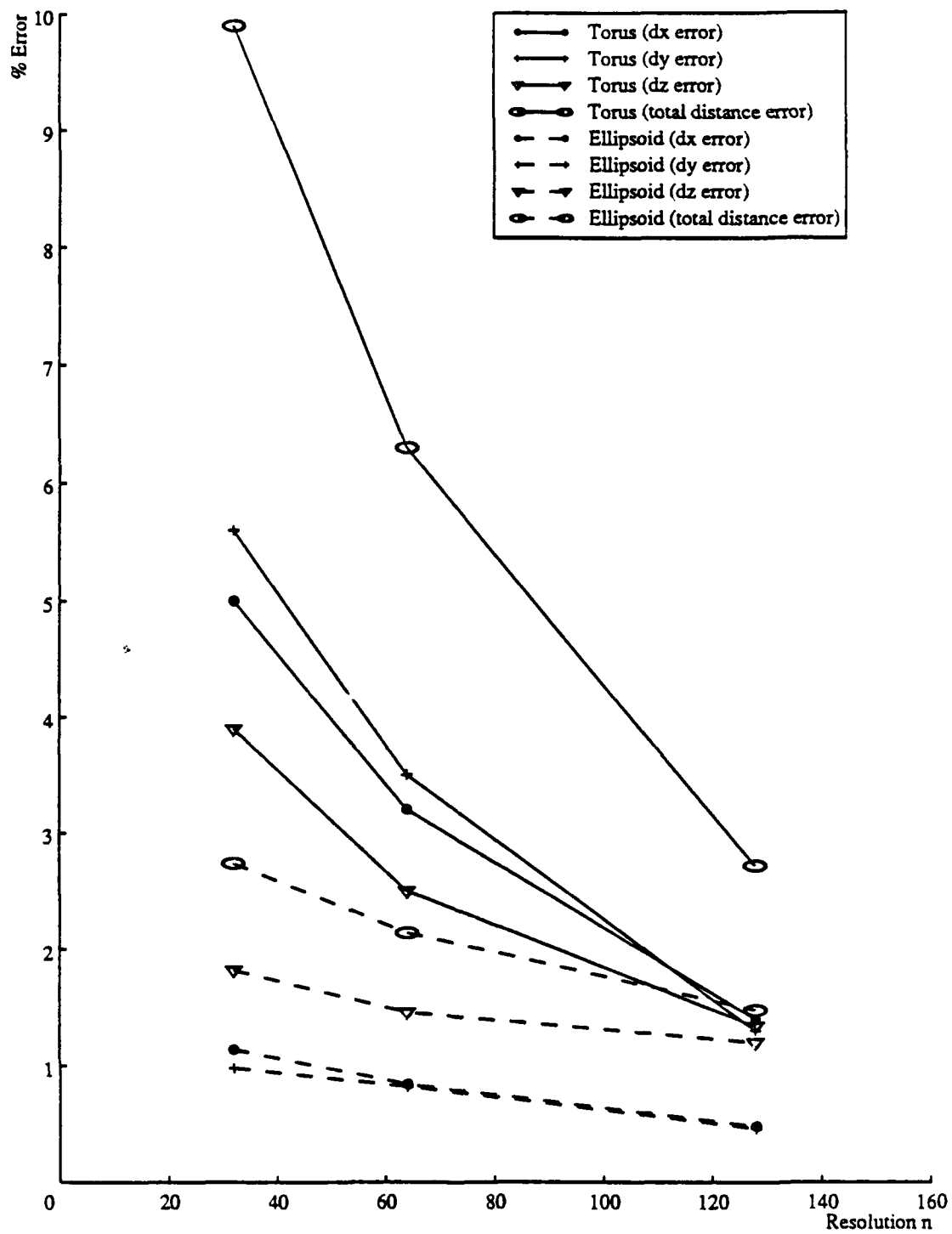
26
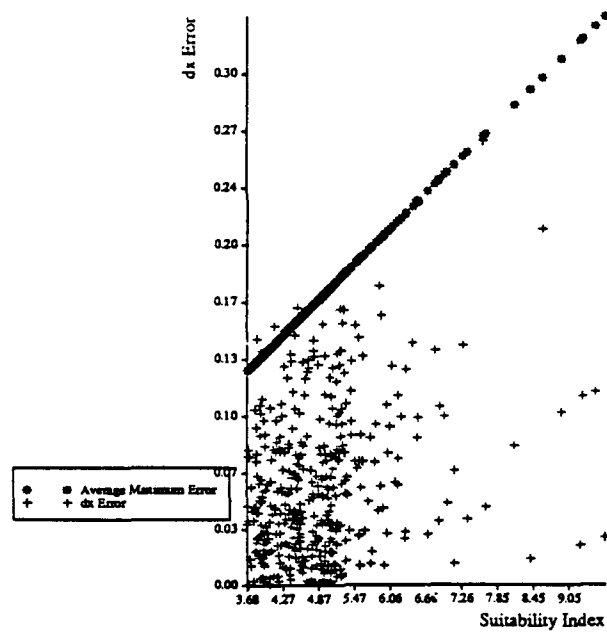
Figure 4.9: Simulation Results for Torus and Ellipsoid

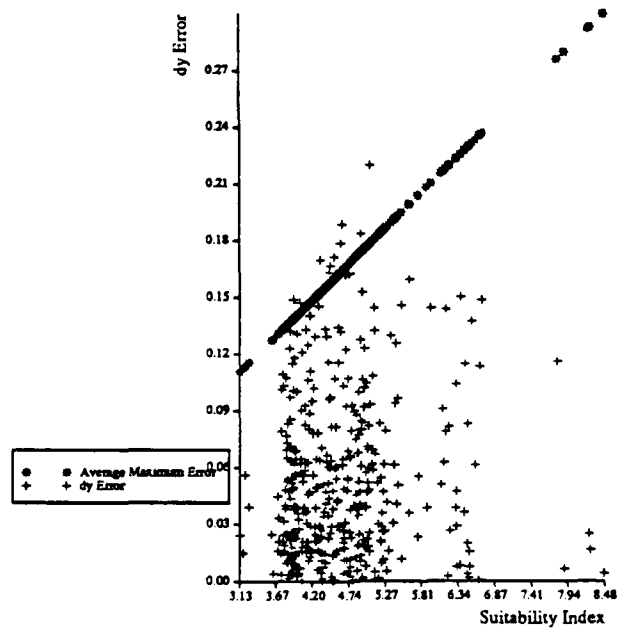Figure 4.10: dx Error vs. View Suitability Index for Model 1 (Angular Error = 3^0)

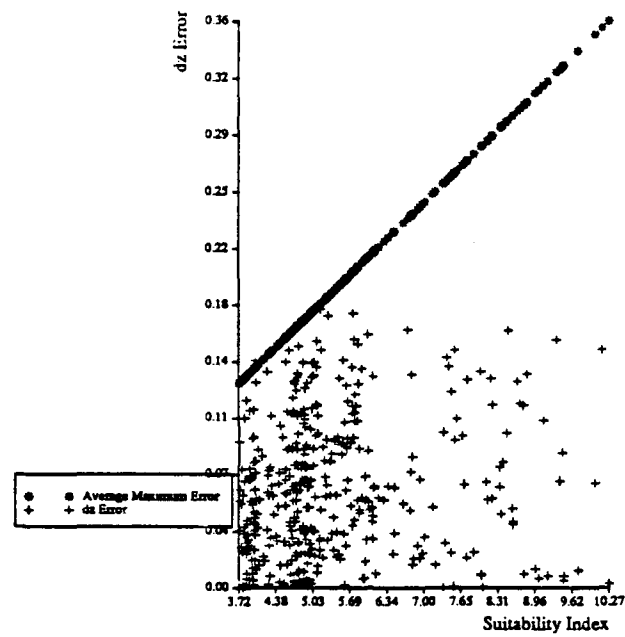Figure 4.11: dy Error vs. View Suitability Index for Model 1 (Angular Error = 3^0)

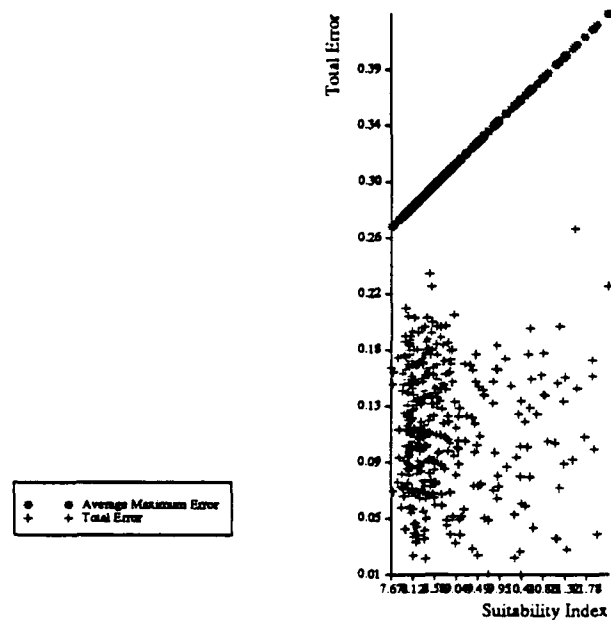Figure 4.12: dz Error vs. View Suitability Index for Model 1 (Angular Error = 3^0)

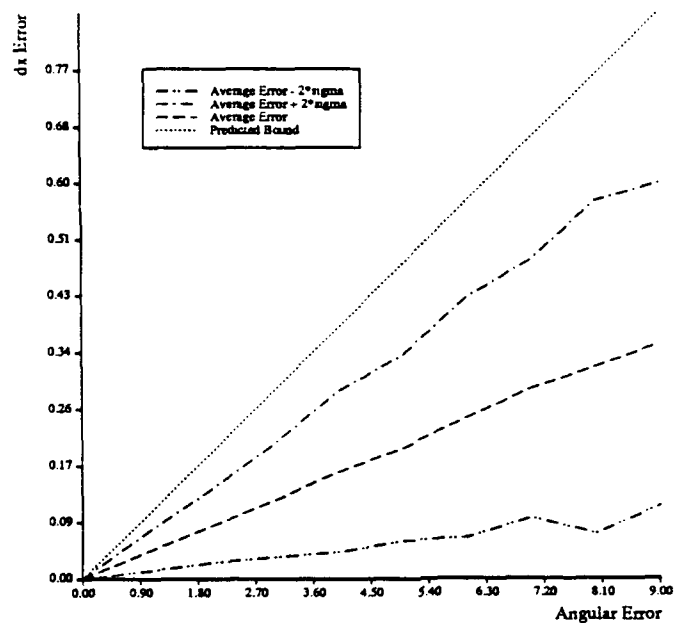Figure 4.13: Total Error vs. View Suitability Index for Model 1 (Angular Error = 3^0)
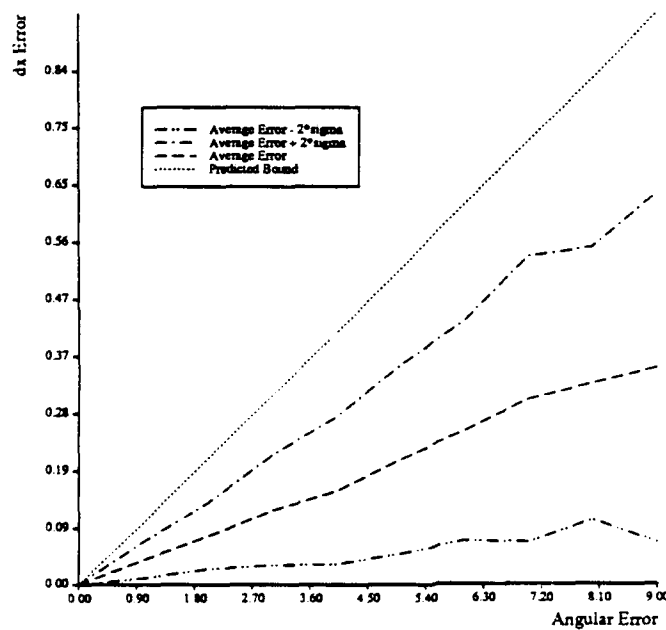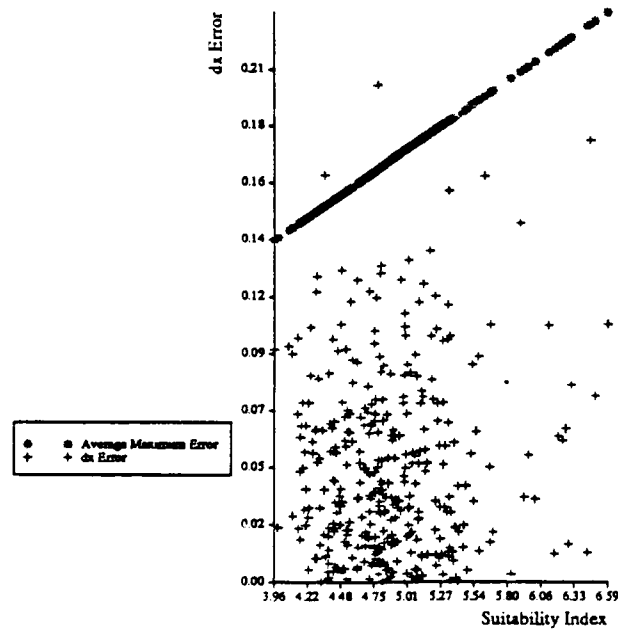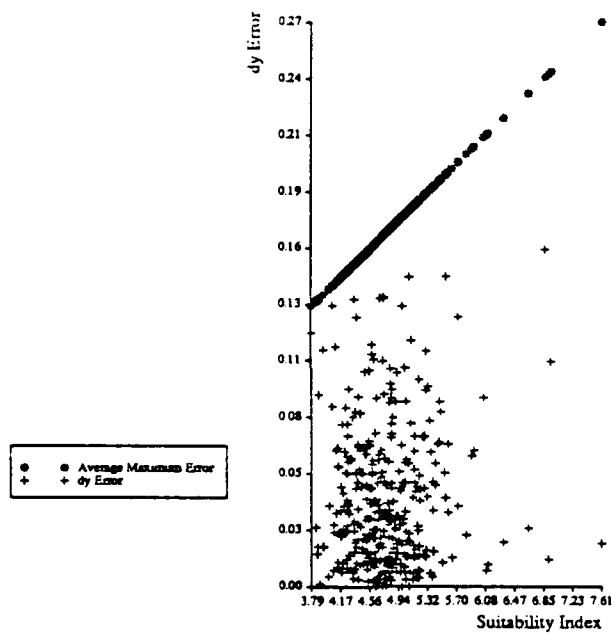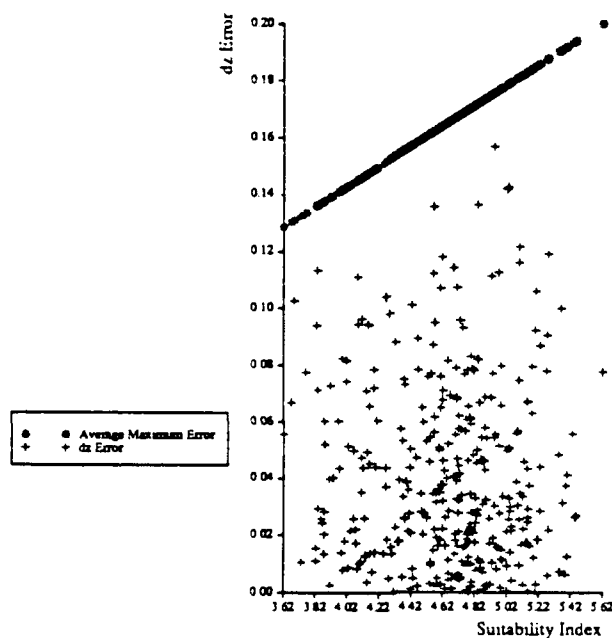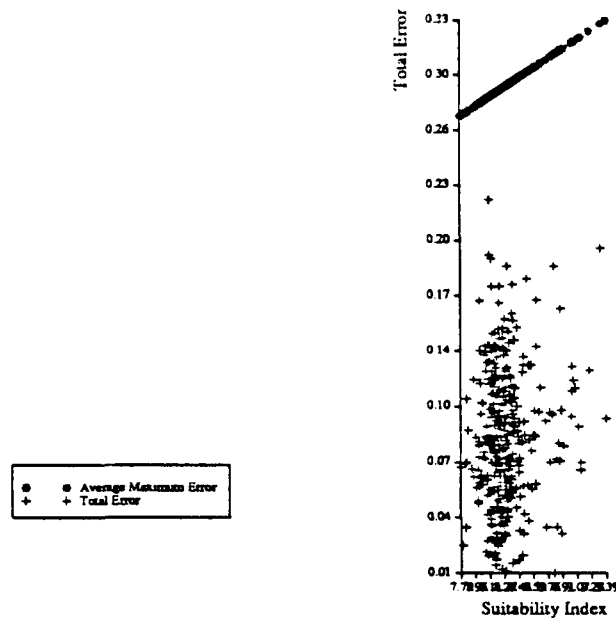
Figure 4.14: Total Error vs. Angular Error for Model 1 ($7.50 \le \Omega_\theta < 8.50$)

Figure 4.15: Total Error vs. Angular Error for Model 1 ($8.50 \le \Omega_\theta < 9.50$)

30
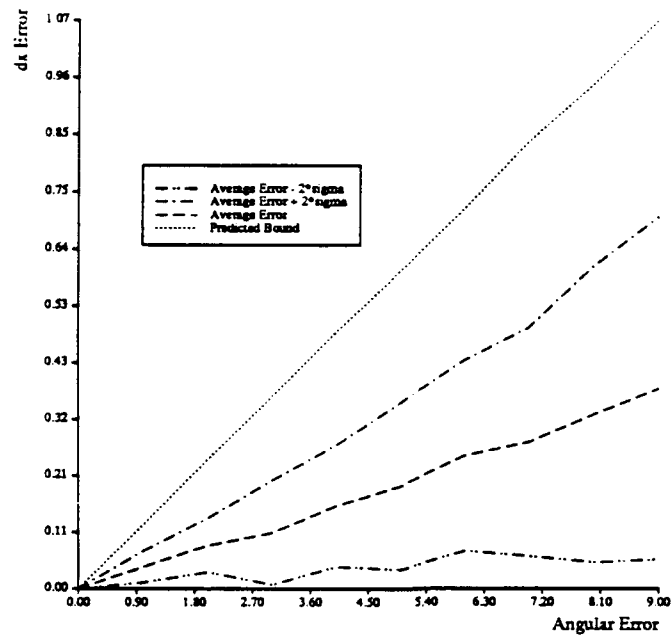
Figure 4.16: Total Error vs. Angular Error for Model 1 ($9.50 \leq \Omega_\theta < 11.50$)

Figure 4.17: dx Error vs. View Suitability Index for Model 2 (Angular Error = 3^0)

Figure 4.18: dy Error vs. View Suitability Index for Model 2 (Angular Error = 3^0)

Figure 4.19: dz Error vs. View Suitability Index for Model 2 (Angular Error = 3^0)

32

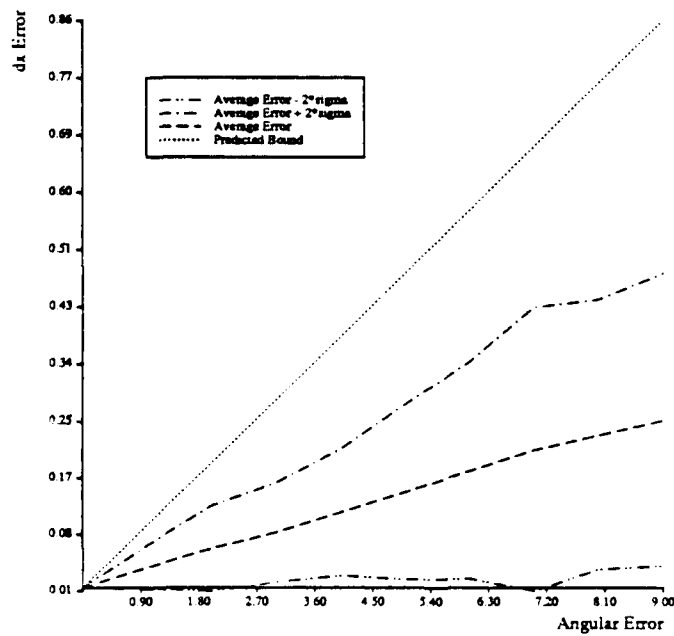Figure 4.20: Total Error vs. View Suitability Index for Model 2 (Angular Error = 3^0)

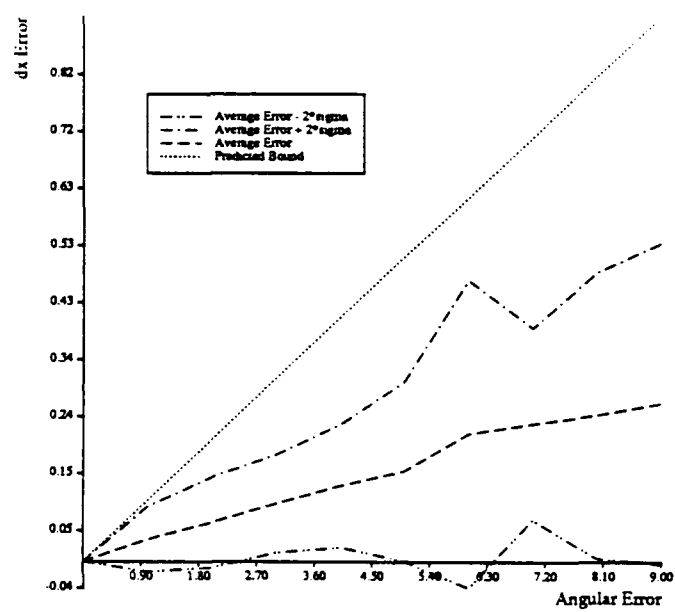Figure 4.21: Total Error vs. Angular Error for Model 2 ($7.50 \leq \Omega_\theta < 8.50$)

Figure 4.22: Total Error vs. Angular Error for Model 2 (8.50 $\leq \Omega_\theta <$ 9.50)

Chapter 5

Experiments Using Real Range Data

To further confirm the validity of the pose recovery technique, experiments involving real range data of two smooth objects were conducted. The two smooth objects are the torus and ellipsoid, whose databases have been created in the simulations earlier.

5.0.1 Implementational Issues

The torus and ellipsoid were crafted out of clay to resemble the models whose databases were created. A light stripe range finder was used to produce a range image of these two objects in various poses and at two different resolutions. The experimental scheme is shown in Fig. 5.1. The resolution of Set 2 range images is twice that for Set 1 images.

5.0.2 Results

The surface maps of the range images taken are shown in Fig. 5.2 (torus - Set 1), Fig. 5.3 (ellipsoid - Set 1), Fig. 5.4 (torus - Set 2), and Fig. 5.5 (ellipsoid - Set 2). The experimental results for these images are summarized in Tables 5.1 and 5.2. Note that all the figures are quoted in percentages of the maximum allowable displacement. In this case, all the numbers are in millimeters.

Again, as for the simulation results, the displacement errors are smaller for Set 2 experiments (which feature higher resolution range images) for both objects. Again the errors in the translation parameters are significantly higher (this time by a smaller factor of 1.5-2) for the torus than those for the ellipsoid.

Despite the fact that the clay models are not exactly the same as the models created in the database, reasonable accuracy could still be attained. Figs. 5.6 and 5.7 compare the actual positions with the calculated positions of the torus and ellipsoid in the range images.
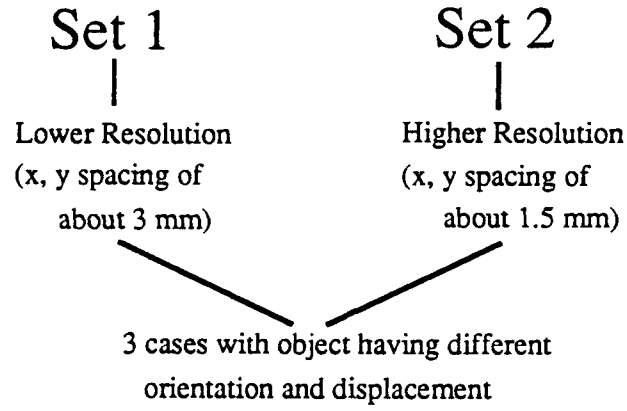
Figure 5.1: Experimental scheme

Case #	Lower Resolution				Higher Resolution			
	$\overline{\epsilon_{d_x}}$	$\overline{\epsilon_{d_y}}$	$\overline{\epsilon_{d_z}}$	$\overline{\epsilon_{d_{xyz}}}$	$\overline{\epsilon_{d_x}}$	$\overline{\epsilon_{d_y}}$	$\overline{\epsilon_{d_z}}$	$\overline{\epsilon_{d_{xyz}}}$
1	1.7	5.9	5.0	8.5	1.4	2.9	4.0	5.4
2	2.6	4.1	7.3	9.5	4.2	2.5	5.6	7.7
3	3.1	4.2	3.6	6.6	3.2	1.4	2.9	5.5

Table 5.1: Experimental Results for Torus

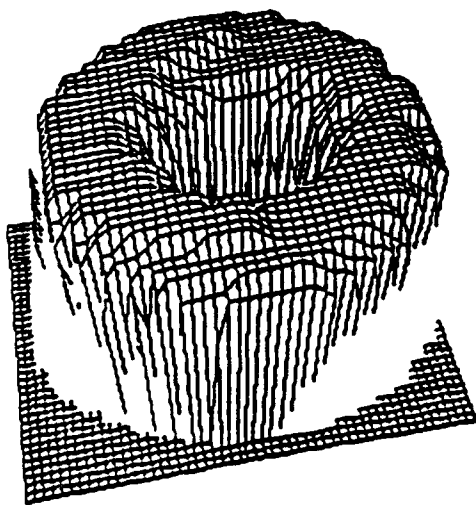| Case #	Lower Resolution				Higher Resolution			
	$\overline{\epsilon_{d_x}}$	$\overline{\epsilon_{d_y}}$	$\overline{\epsilon_{d_z}}$	$\overline{\epsilon_{d_{xyz}}}$	$\overline{\epsilon_{d_x}}$	$\overline{\epsilon_{d_y}}$	$\overline{\epsilon_{d_z}}$	$\overline{\epsilon_{d_{xyz}}}$
1	0.9	1.4	3.2	3.7	0.9	3.1	1.6	3.6
2	0.4	2.1	4.9	5.4	0.9	4.1	0.2	4.2
3	1.3	2.7	2.1	3.9	1.6	0.5	1.9	2.6

Table 5.2: Experimental Results for Ellipsoid
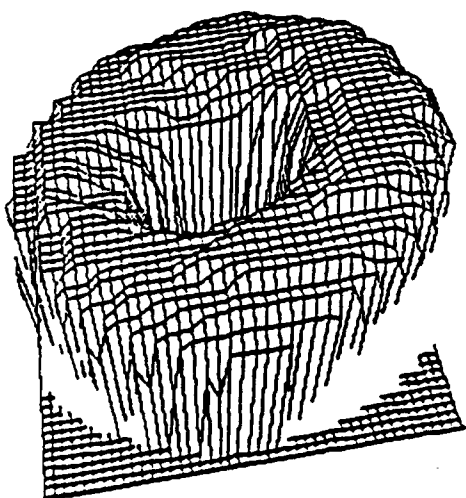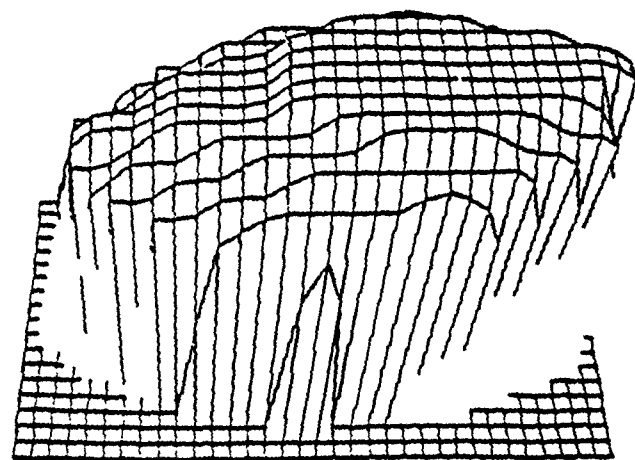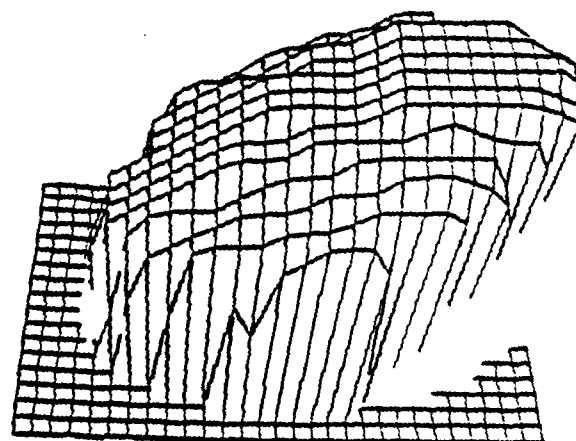
Torus : Case 1   Torus : Case 2
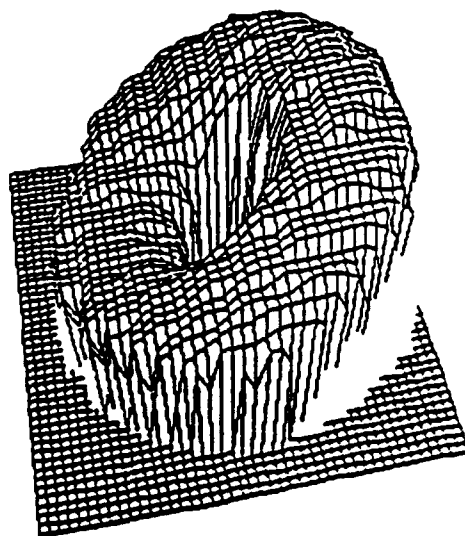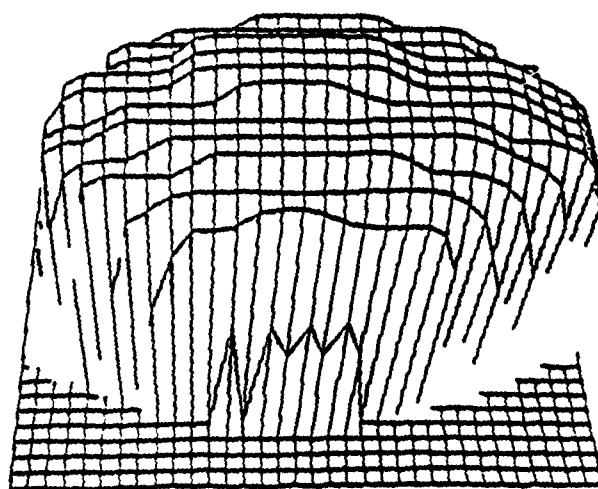
Torus : Case 3

Figure 5.2: Surface maps for the torus at three poses (Set 1)
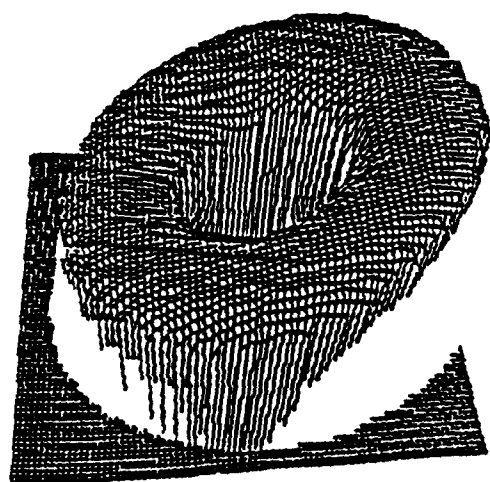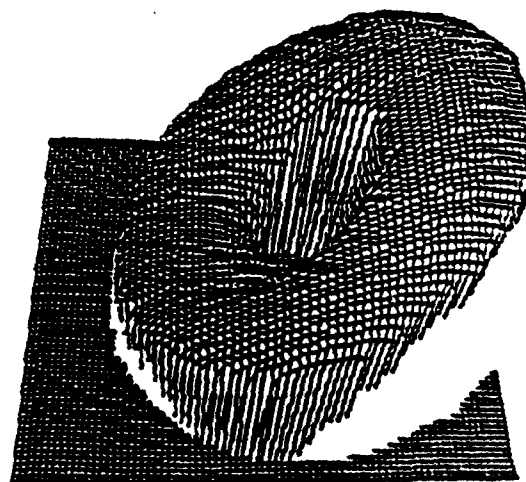
Ellipsoid : Case 1

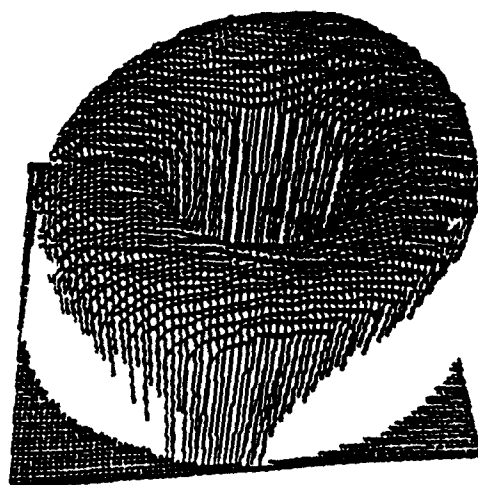Ellipsoid : Case 2

Ellipsoid : Case 3

Figure 5.3: Surface maps for the ellipsoid at three poses (Set 1)

Torus : Case 1

Torus : Case 2

Torus : Case 3

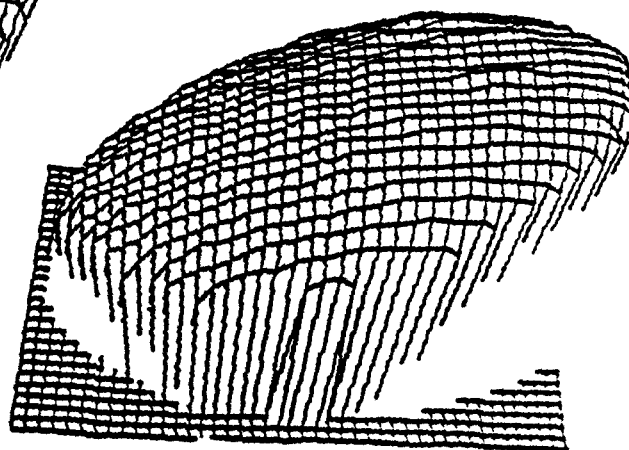Figure 5.4: Surface maps for the torus at three poses (Set 2)
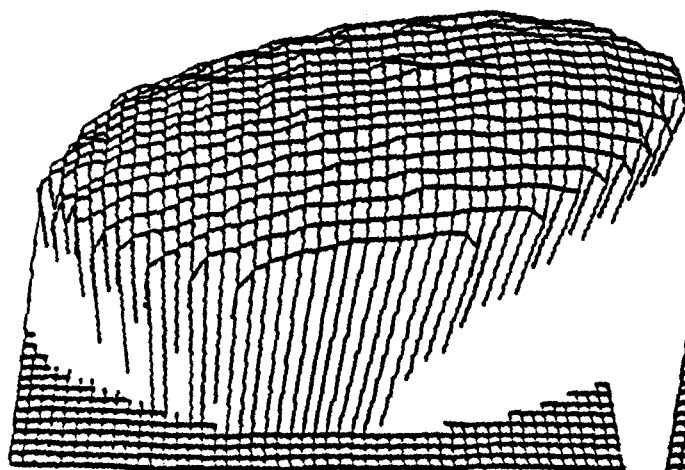
Ellipsoid : Case 1

Ellipsoid : Case 2
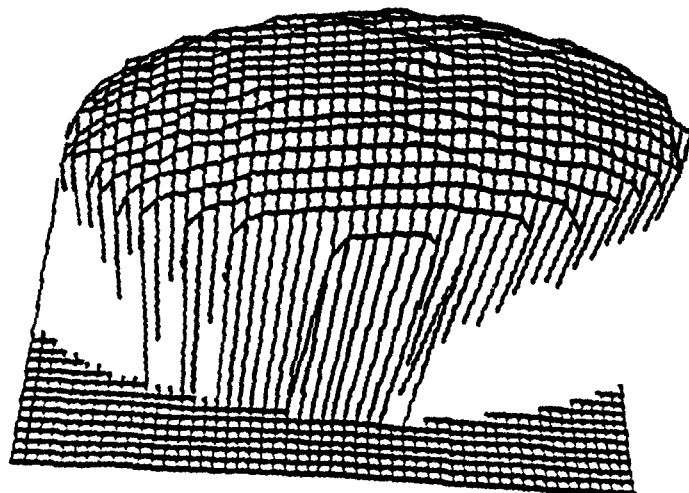
Ellipsoid : Case 3

Figure 5.5: Surface maps for the ellipsoid at three poses (Set 2)

Figure 5.6: Top, Left: Intensity image of torus (Set 2, Case 1); Top, Right: Superimposed model (Set 2, Case 1); Bottom, Left: Intensity image of torus (Set 2, Case 2); Bottom, Right: Superimposed model (Set 2, Case 2)

Figure 5.7: Top, Left: Intensity image of ellipsoid (Set 2, Case 1); Top, Right: Superimposed model (Set 2, Case 1); Bottom, Left: Intensity image of ellipsoid (Set 2, Case 2); Bottom, Right: Superimposed model (Set 2, Case 2)

Chapter 6

Conclusions

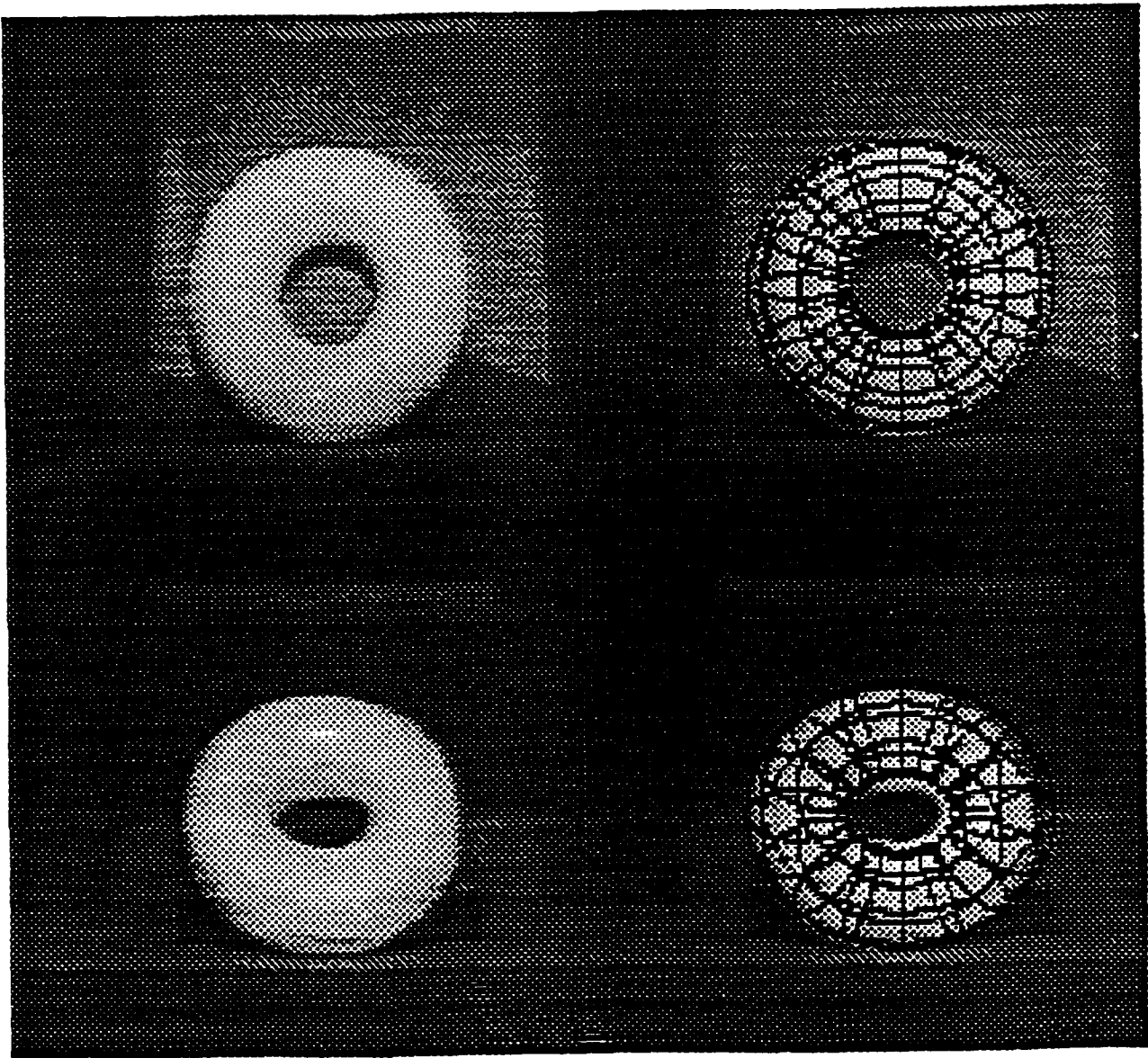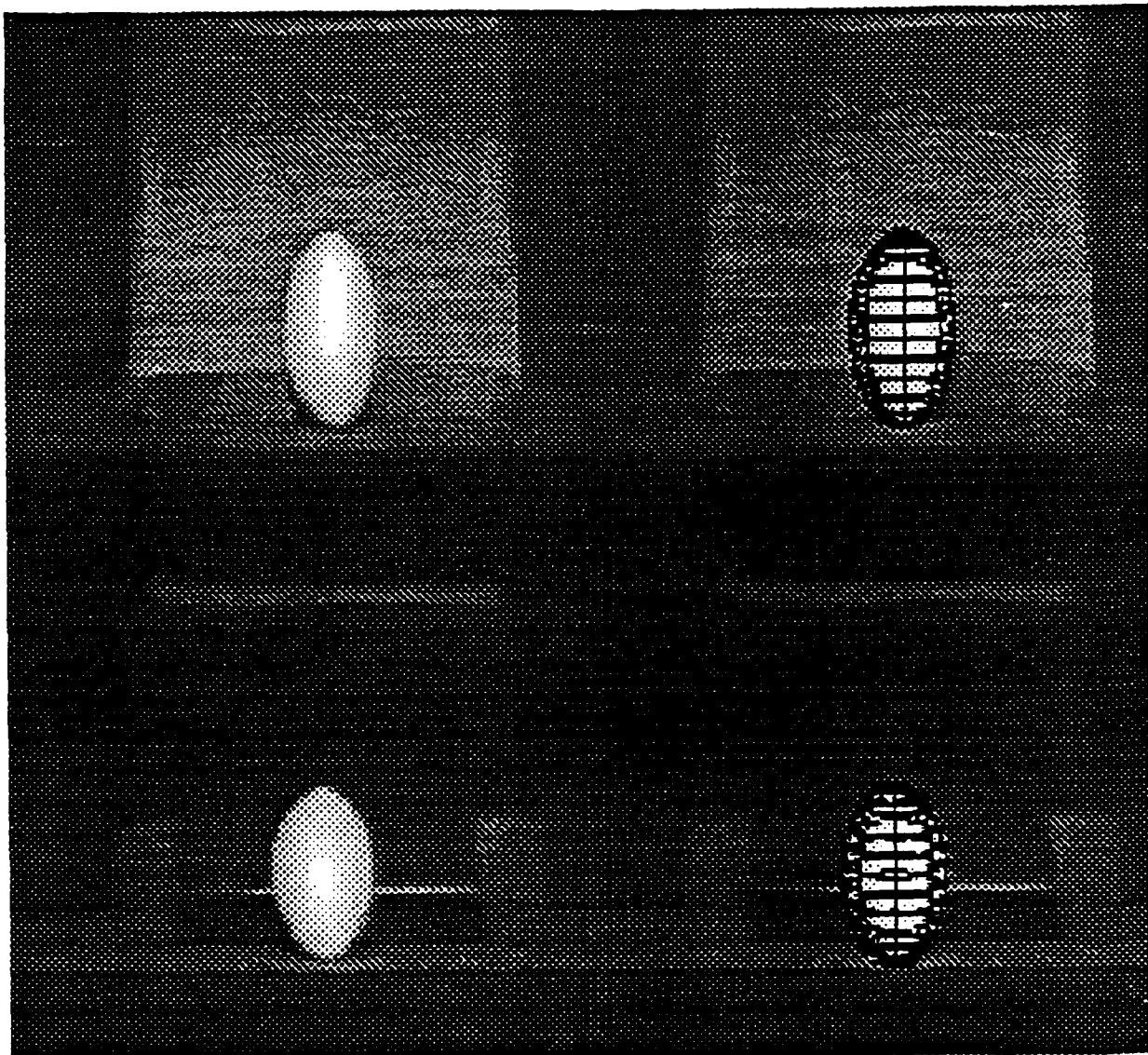A new variant of the EGI representation which encodes object face position has been described. Known as the Complex Extended Gaussian Image (CEGI), it is a histogram of spatial orientation in which each weight associated with a normal is a complex number. The normal distance of the face from the predefined origin is encoded as the *phase* of the weight while the magnitude of the weight is the visible area of the face.

The CEGI provides a *global* method of extracting both the orientation and translation of a detected object with respect to a stored model or prototype. The method of determining the translation parameters is simple, being based on the least squares formulation. The CEGI effectively decouples the orientation and translation determination into two separate problems. The orientation of the object can be determined by first calculating the magnitude distribution of its CEGI before matching the resulting distribution with those in the database. This operation is exactly the same as that using the conventional EGI. The translation parameters can subsequently be estimated by comparing the complex weight phases.

A significant advantage of this scheme is that it works for both polyhedral and smooth objects. It can be used without the need to know the type of object a priori. On the other hand, the polyhedral object whose translation parameters need to be determined should be relatively complex, in terms of the number of faces and distribution of surface normals. The more the number of faces and discrete normal directions, the more accurate the resulting estimated displacement is likely to be. In addition, the accuracy of estimated translation parameters for smooth objects is influenced by the degree of concavity. In experiments using actual data collected from smooth objects, accuracies of up to 3% is possible using the CEGI.

Based on error analysis, the accuracy of the derived translation parameters is sensitive to the angular error of the surface normals, the magnitude of the actual translation parameters, and the distribution of the surface normals. An index which can be used as an indication of the *bound* on the translation parameters has been derived and is called the view suitability index. It has been shown through simulations that the mean of the translation errors is linear with normal angular error.

The error analysis shows that the view suitability index can be used as a measure which bounds extracted translation parameters. The CEGI, whose distance information is encoded in

the weight phase, has been shown to be an effective means of determining object displacement. In addition, it is capable of distinguishing between the convex object and most other concave objects whose EGI's are identical to that of the convex object. Finally, the CEGI can be used for any reasonably complex objects, polyhedral or smooth.

Chapter 7

Acknowledgments

Chapter 8

References

[1] Balakumar, P. et al. *VANTAGE: A Frame-Based Geometric Modeling System - Programmer/User's Manual.* CMU, December 1988.

[2] P.J. Besl and R.C. Jain. Three-Dimensional Object Recognition. *Artificial Intelligence*, 17(1):75–145, March 1985.

[3] R.C. Bolles, P. Horaud, and M.J. Hannah. 3DPO : A Three-Dimensional Part Orientation System. *1st Int'l Symposium on Robotic Research*, pages 413–424, 1984.

[4] C. Dane and R. Bajcsy. Three-Dimensional Segmentation Using the Gaussian Image and Spatial Information. *Proc. Int'l Conf. on Pattern Recog. and Image Proc.*, pages 54–56, August 1981.

[5] T.J. Fan, G. Medioni, and R. Nevatia. Matching 3-D Objects Using Surface Descriptions. *Int'l Conf. on Robotics and Automation*, pages 1400–1406, April 1988.

[6] O.D. Faugeras. New Steps Toward a Flexible 3-D Vision System for Robotics. *Proc. Int'l Conf. Pattern Recog.*, pages 796–805, July 1984.

[7] O.D. Faugeras, N. Ayache, and B. Faverjon. A Geometric Matcher for Recognizing and Positioning 3-D Rigid Objects. *Proc. Artificial Intelligence Applications*, pages 218–224, December 1984.

[8] O.D. Faugeras and M. Hebert. A 3-D Recognition and Positioning Algorithm Using Geometrical Matching Between Primitive Surfaces. *Proc. Int'l Joint Conf. Artificial Intell.*, pages 996–1002, August 1983.

[9] M. Hebert and J. Ponce. A New Method for Segmenting 3-D Scene into Primitives. *Proc. Int'l Conf. on Pattern Recog.*, pages 836–838, October 1982.

[10] B.K.P. Horn and K. Ikeuchi. The Mechanical Manipulation of Randomly Oriented Parts. *Scientific American*, August 1984.

[11] K. Ikeuchi. Recognition of 3-D Objects Using the Extended Gaussian Image. In *Proc. of Seventh IJCAI*, pages 595–600, 1981.

[12] K. Ikeuchi. Determining Attitude of Object from Needle Map Using Extended Gaussian Image. Technical Report AI Memo 714, MIT, 1983.

[13] K. Ikeuchi and B.K.P. Horn. Numerical Shape from Shading and Occluding Boundaries. *Artificial Intelligence*, 17:141–185, 1981.

[14] J.J. Little. An Iterative Method for Reconstructing Convex Polyhedra from Extended Gaussian Images. *Proc. of the National Conf. on AI*, pages 247–250, August 1983.

[15] J.J. Little. Recovering Shape and Determining Attitude from Extended Gaussian Image. Technical Report TR 85-2, Univ. of British Columbia, April 1985.

[16] H. Minkowski. Allgemeine Lehrsatze uber die konvexe Polyeder. *Nachr. Ges. Wiss. Gottingen*, 1897.

[17] S. Moni. A Closed-Form Solution for the Reconstruction of a Convex Polyhedron from its Extended Gaussian Image. *Int'l Conf. on Pattern Recog.*, 1:223–226, June 1990.

[18] R. Nevatia and T.O. Binford. Description and Recognition of Curved Objects. *Artificial Intelligence*, (8):77–98, 1977.

[19] J. Ponce and D.J. Kriegman. On Recognizing and Positioning Curved 3-D Objects From Image Contours. *Proc. Image Understanding Workshop*, pages 461–470, May 1989.

[20] J.W. Roach, J.S. Wright, and V. Ramesh. Spherical Dual Images: A 3D Representation Method for Solid Objects that Combines Dual Space and Gaussian Spheres. *Proc. CVPR*, pages 236–241, June 1986.

[21] Tanaka, H. et al. Parallel Polyhedral Shape Recognition. *Proc. Computer Vision and Pattern Recognition*, June 1985.